1

Ground-Wave Propagation

with **FUNDA AKLEMAN**

1.1 INTRODUCTION

In general, propagation through inhomogeneous media, with variable and imperfect boundaries is simulated in this chapter. Although ground waves are of main interest, numerical simulators presented here are quite general and applicable to, for example, propagation through transmission lines, microstriplines, coaxial cables, waveguides, optical films, etc.

The frequency bands of interest are MF (medium frequencies, 300 kHz to 3 MHz), HF (high frequencies, 3 - 30 MHz), VHF (very high frequencies, 30 - 300 MHz), UHF (ultra high frequencies, 300 MHz to 1 GHz), and MW (microwaves, 1 GHz and above).

At frequencies between 3 kHz and 30 MHz, two types of electromagnetic (EM) wave propagation between two points on or above the earth are possible: ground wave propagation and indirect sky wave (ionospheric wave). Ground wave propagation is affected by the tropospheric variations (neutral atmosphere) as well as ground characteristics. Sky wave is reflected from the ionosphere back to the earth at appropriate frequencies and angles of incidence giving rise to long-range propagation. Although the ionosphere acts as a reflector up to frequencies of a few megahertz, it becomes more penetrable for EM waves above 30 MHz as the operating frequency increases; and at a critical frequency, no reflection towards ground occurs. Therefore, propagation along the earth via sky wave is not possible at VHF and upper frequencies. In this chapter, the ground wave propagation is of main interest for the frequency bands given above; and the characteristics of the ionosphere, which is composed of a number of ionized regions, are not considered here.

Ground waves have three components: direct waves, ground-reflected waves, and surface waves. The model environment is a spherical earth with various ground characteristics, above which exists a radially inhomogeneous atmosphere. Having an excitation and observer anywhere on or above the ground, this model has served as a canonical problem. The problem is very complex and neither a full-wave, observable-based, numerically computable analytical solution nor a 3D, generally applicable, numerical solution has appeared yet. Instead, analytical approximate and 2D numerical solutions, valid under different parameter regimes, together with some hybridized solutions, are being used.

The physical characteristics of the propagation depend on many parameters, such as the operating frequency, medium parameters, grazing angle, transmitter and receiver locations, and the geometry (boundary conditions, BC) between them. Some characteristics of the ground wave propagation can be listed as:

- At MF and lower HF, ground-wave propagation is dominated by the surface wave. As long as the transmitter and receiver are close to the surface, direct and ground reflected waves cancel each other and only surface waves can propagate. The earth's surface electrical parameters are important in reaching longer ranges. Sea surface is a good conductor, but ground is a poor conductor at these frequencies. For example, with the same transmitter and receiver characteristics, a 5 MHz signal, which reaches 400-km range over the sea, can only reach up to 40 - 50-km range over the poor ground. Typical electrical parameters (σ, conductivity, ε_r, relative permittivity) are listed in Table 1.1.

- At MF and lower HF, propagation is possible up to the 400 - 500-km range. MF are used for long- and medium-wave radio broadcasting. Lower HF is used for long-range marine communication and HF surface-wave radars. Propagation beyond the line-of sight (LOS, a straight line from transmitter that is tangent to the earth's surface) is possible at these frequencies via surface waves and/or sky waves.

- Surface waves are hardly excited and coupled to the surface, when the transmitter is many wavelengths (e.g., 5λ to 10λ) above the ground. When excited and coupled, they exponentially decay with height; therefore surface waves are rarely used above 10 - 15 MHz.

- At VHF and above (i.e., VHF, UHF and MW), propagation is limited by the LOS, because surface-wave contribution becomes negligible at these frequencies and the ground wave is then known as the space wave, which is the sum of direct and ground reflected waves. For near grazing path, the complex reflection coefficient of the ground for both horizontal and vertical polarization approaches –1, which is appropriate to assume ground as perfectly conducting.

- At VHF, propagation beyond the LOS is still possible by means of diffracted components (typically 5 km to 20-km range beyond obstacles)

Table 1.1: Typical ground parameters

Ground	**σ [S/m]**	**ε_r**
Sea	5.0	80.0
Medium ground	0.01	15.0
Poor ground	0.001	7.0

Today's communication systems and radars are mostly used within multi-area, multi-sensor, land-based, maritime and/or air-based complex integrated systems (such as an integrated maritime surveillance system or integrated early warning system against tactical ballistic missiles, etc.). Research towards the development and to the performance evaluation of such systems requires powerful computer simulation tools and can only be done via these simulators. Some requirements, related to current integrated system simulations, are as follows:

- Modeling of propagation characteristics and path loss predictions in integrated surveillance system simulations, where optical, microwave, and HF radars are used

- Service planning, in rural and urban locations, for mobile communication systems using 900-MHz and 1.8-GHz systems and for FM radio stations

- Sensor location and service planning for Intelligent Traffic Management Systems (ITMS) in a complicated and densely occupied urban metropolis

- Control and/or detection of very low altitude missiles, camouflaged by the local terrain profile up to the target

- Knowledge of propagation characteristics to overcome problems related to emerging radar technologies (HF and VHF radars), ..., etc.

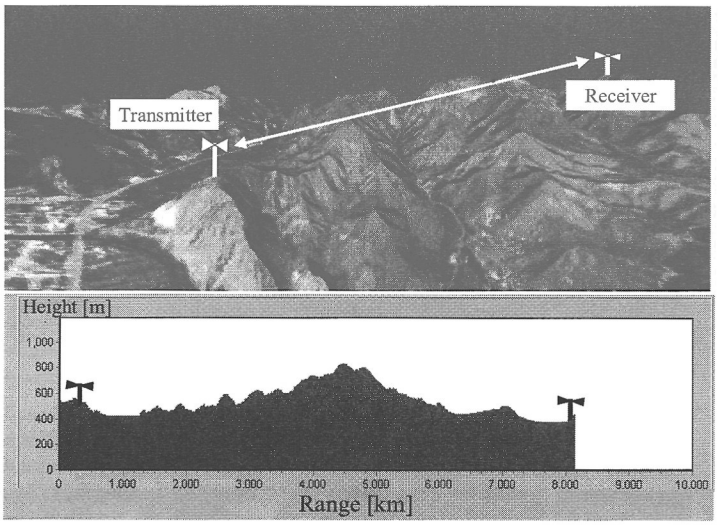

Figure 1.1: *A typical digital map and the height/range function for a chosen propagation path*

In real-world systems, such as those exemplified above, the problem of determining the propagation characteristics between any two selected points (e.g., a communication transmitter and receiver) can best be addressed via an accurate and versatile simulation model. Such a simulator is expected to accept the characteristics of the propagation environment as input (digitized map of the non-flat terrain, as seen in Fig.1.1, ground cover types, parameters of the troposphere, etc.) and provide wave propagation characteristics as output, in a nearly real-time basis. Clearly such a simulation tool would be indispensable to the decision-maker (service planner, site engineer, or the leader of a small military ground contingent) and it has therefore been a continuing challenge to develop a simulator, which satisfies these requirements. The challenge here is to parameterize this complex system in terms of the variety of wave processes that operate there.

1.1.1 Historical Overview

In the review article by J. R. Wait [1] the ancient and modern history of EM ground wave propagation is outlined, and the feature article by N. DeMinco [2] contains a wide-ranging survey of radio wave propagation and antenna modeling. Here we will present a brief history of the investigations related to wave propagation over the earth. For a more detailed account on this subject the reader is referred to the review paper of the J. R. Wait [1].

Beginning with the original investigations of Heinrich Hertz, the influence of the interference caused by the obstacles in the path had been an important subject and then in 1899 Marconi investigated the weakening of the field strength when a hill was located between transmitter and receiver. Early conjectures were that the signal was guided in some fashion by the air - earth boundary, and at that time the possible existence of the ionosphere was also broached. At the turn of the century, the presence of the earth had been a key factor to be reckoned with, and this was the beginning of the subject that is now called "ground-wave propagation."

In 1907, Zenneck analyzed the possibility that the air - earth interface supported a surface wave with low attenuation. Although the guiding-wave mechanism of the air - earth interface seemed to be a leading subject to explain the radio wave transmission over long distances, Sommerfeld took the lead to put the question on a firm mathematical basis. His analysis dealt with the problem of determining the fields of electric and magnetic dipoles located in the insulating half-space over a conducting half-space as well as dipoles located in the planar interface. In 1926, Sommerfeld corrected his original formulation. In 1930s, there was activity on the question of the validity of the Sommerfeld theory, including the modified 1926 version. Pol and Niessen confirmed that the physical form of the Sommerfeld 1926 version was correct. There has been a great deal of discussion in the literature, for the past 50 years or more, on the form the theory should take for the general case of raised terminals. Norton developed an improved form for the Hertz potential for arbitrary heights. J. R. Wait [3] and his former colleague, R. J. King proposed various forms that had the uniform property of reducing exactly to geometrical optics at higher elevation angles. It is pointed out that Norton formulation of surface wave is to be defined as the difference between the total wave field and the easily computed space-wave component (sum of direct and ground-reflected wave) or GO field. R. King has also employed the surface-impedance model, in an independent integral-equation solution.

In order to deal with the actual physical world, a spherical earth model has to be used. In 1918, G. N. Watson began with the classical harmonic series solution for a dipole, in the presence of a homogeneous sphere of radius a with the electrical properties conductivity σ, dielectric permittivity ε, and magnetic permeability μ. The surrounding medium was accepted as free space. Although the solution involving spherical Bessel functions of integer order was mathematically correct, convergence properties were poor. Watson's first step was to represent the series by a contour integral that enclosed the real axis of the complex wavenumber plane, and then Watson wrapped the contour around a manageable number of complex poles, which provided a highly convergent residue series in the shadow region. The improved spherical-earth modal residue series solution is explained in detail in [3,4]. The mixed-path (i.e., land - sea transition) theory [5] as well as irregular terrain concepts [6,7] are also analyzed with analytic approximate approaches by various researches (see [1] for reference list).

1.1.2 Available Approaches

Problem-matched analytic approximate approaches as well as purely numerical techniques have been used and are still being developed to better understand and model wave propagation over a non-flat terrain covered with various ground cover types. Analytic models listed below assume a smooth spherical earth (and/or its earth-flattened approximate equivalent) with various smooth ground characteristics, a radially inhomogeneous atmosphere above and excitation by a vertical or a horizontal electric dipole on or above the earth's surface.

1. The Norton formulation, which extracts from a wavenumber spectral integral representation a ray-optical asymptotic approximation [8].

2. The Wait formulation, which restructures the spectral integral as a series of normal modes propagating along the earth's surface [3].

3. The Ishihara - Felsen formulation, which combines ray fields and mode fields in a self-consistent hybrid scheme [9,10], which however, is valid under less general conditions than those of options 1 and 2 individually.

4. The hybrid algorithm, WAVEPROB, which combines Norton and Wait solutions in an efficient manner to extend the range of validity of options 1 and 2 [11].

5. The adiabatic and intrinsic mode formulations, which extend analytic modal solutions to media with transverse as well as longitudinal variations [12,13].

6. The numerical solution of the parabolic equation (PE) that is derived in an approximate sense neglecting the back-scattered field (one-way propagation) and is most directly applicable within a narrow range of angles between the propagation direction and range (i.e., paraxial approximation) (see [14] for historical review and references for various PE approaches).

7. A split-step Padé PE method for problems involving large angles between propagation direction and range [14].

8. An improved PE method for impedance (Cauchy-type) boundary conditions [14,15].

9. The hybrid ray - PE method, which addresses transitional effects in option 3 [16].

10. A hybrid (finite difference PE) – (surface Green's function) method to account for propagation loss over mixed paths [14,17].

11. A horizontal PE method for the rigorous extension of standard PE solutions to large transverse spatial domains [14].

12. The FDTD-based wave propagator (TDWP), which simulates and traces broadband pulse propagation over long distances [18,19].

13. The TLM-based wave propagator (TLM-WP), which simulates and traces broadband pulse propagation over long distances [20].

14. Simplified Deygout solution for multiple knife-edge diffraction [21] (more sophisticated diffraction models representing the terrain profile as a succession of knife-edges, wedges, cylinders or flat strips are also available [22,23]. Another important family of models uses an integral equation formulation [6,7], which can be simplified by paraxial approximation [24]. All of these techniques assume propagation in a homogeneous or linear atmosphere).

In dealing with the propagation requirements listed above, it is essential to understand propagation characteristics over spherical earth's surface such as (i) energy spread because of curvature effects, (ii) wave scattering because of irregular terrain, (iii) guiding as well as anti-guiding effects because of refractivity variations, etc. Although it is a source-driven (i.e., a Green's function) problem in 3D spherical co-ordinates, because of the azimuthal symmetry met in almost all practical applications this problem can be reduced to 2D and using appropriate transformations the natural co-ordinates of the problem can be converted into normalized Cartesian co-ordinates (see Fig. 1.2) [11,19]. Detailed reviews of these radiowave propagation problems can be found in [1,2,25 - 27].

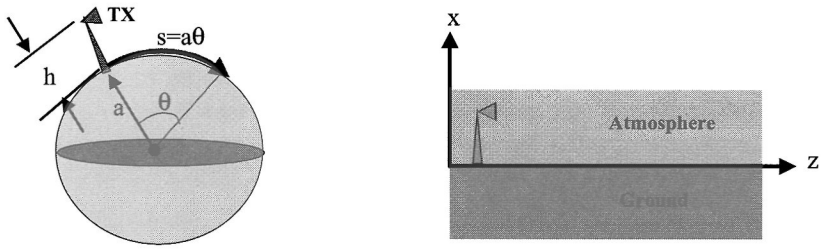

Figure 1.2: *The geometry of the ground-wave propagation problem in (a) spherical coordinates and (b) normalized Cartesian coordinates.*

1.1.3 The Lower Atmosphere

Ground wave propagation through atmosphere (up to nearly 100 GHz) is affected by oxygen and water-vapor molecules. The air can be considered as a non-dispersive medium and can be represented by its refractive index ($n = \sqrt{\varepsilon_r}$). The refractivity of the propagation medium should be well understood, since non-flat terrain and/or earth's curvature may also be implemented via refractivity in most of the analytical as well as numerical approaches. Refractive index of the air is very close to unity (typically about 1.0003); therefore, it is customary to use the refractivity *N*, defined as

$$N = (n-1)\times 10^6 \tag{1.1}$$

were N is dimensionless, but is measured in "N units" for convenience. N depends on the pressure P (mbar), the absolute temperature T (°K) and the partial pressure of water vapor e (mbar) as [18],

$$N = 77.6\frac{P}{T} + 3.73\times10^5\frac{e}{T^2} \tag{1.2}$$

which is valid in earth - troposphere waveguides and can be used in ground wave propagation modeling. If the refractive index were constant, radio waves would propagate in straight lines. Since n decreases with height, radio waves are bent downward toward the earth, so that the radio horizon lies further away than the optical horizon. It should be noted that the radio horizon effect is taken into account either by using N with the effective earth radius a_e, or by introducing a fictitious medium where N is replaced by the modified refractivity M,

$$M = N + \frac{x}{a}\times10^6 = N + 157x \tag{1.3}$$

with the height x given in kilometers. In (1.3)

$$a = 6378 \text{ km}, \quad \frac{10^6}{a} = 157 \text{ and } \quad \frac{\partial M}{\partial x} = \frac{\partial N}{\partial x} + 157 \tag{1.4}$$

For the standard atmosphere (i.e., for a vertical linearly decreasing refractive index), N decreases by about 40 N unit/km while M increases by about 117 N unit/km. Sub-refraction (super-refraction) occurs when the rate of change in N with respect to height (i.e., $\partial N / \partial x$) is less (more) than 40 N unit/km.

A linearly decreasing (increasing) vertical refractive index variation forces a wave trap near (diverge from) the earth's surface while propagating. Similar effects are also caused by concave and convex surfaces. Therefore, there is an analogy between refractive index and surface geometry in terms of propagation effects. By using this analogy, te earth's curvature effect is included into the refractive index of the air. The earth's curvature effect is equivalent to a vertical refractivity gradient of 157 N unit/km (i.e., linear vertical increasing refractivity profile). As stated in the previous paragraph, standard atmosphere, together with te earth's curvature, is represented by a vertical refractivity gradient of 117 N unit/km.

1.1.4 Summary

Norton and Wait formulations parameterize the propagation process in terms of different phenomenological models; their ranges of validity, accuracy, rate of convergence, etc., depending on such problem parameters as operational frequencies, source/observer locations, and the physical propagation environment, differ as well, with particular impact on computations. This has led to a new hybrid WAVEPROB algorithm [11], which seeks to combine the best features of the Norton and Wait algorithms in an efficient, adaptive format, with dynamic prediction of the critical height, range, frequency, and number of necessary roots in the algorithm that switches from one method to the other.

Either by using ray-mode theories separately or by using WAVEPROB, one may deal with smooth-boundary problems, such as [11,25]

- Surface wave path loss or field strength variation with respect to range (especially beyond the horizon and when both transmitter and receiver are on the surface).

- Range and/or height propagation variations in interference regions (i.e., when transmitter and receiver are above the surface and within the line-of-sight (LOS)).

Ray-mode and their hybridized techniques cannot handle problems, such as

- Propagation over rough surface terrain (note that roughness capability can be added to WAVEPROB, in an approximate sense, via modification of the surface reflection coefficient; the Rayleigh roughness criterion, which is based on the phase difference between two nearby reflections of the same incident wave due to surface height changes, may be used for this purpose [11]).

- Propagation through surface and/or elevated ducts formed by inhomogeneous vertical as well as horizontal atmospheric conditions (note that analytic formulations are based on a *coordinate separable* model over a smooth spherical earth with standard atmosphere).

Although height gain functions in mode theory [3] can be used to account for transmitter/receiver heights, it is difficult to deal with receiver heights in diffraction regions (beyond LOS) because of numerical problems in calculating higher-order terms in the series representation of Airy functions [26]. Nevertheless, analytic approximate solutions are important because they parameterize a problem in terms of wave phenomenologies, such as rays and modes, provided that the actual problem does not deviate substantially from the analytic prototype.

The Split-Step Parabolic Equation propagator (SSPE) and recently introduced time-domain wave propagators TDWP and TLM-WP are very promising, since they all can handle propagation over a realistic spherical earth's surface (including non-flat terrain profile as well as vegetation modeled as a surface impedance) above which lies an atmosphere with a transverse as well as longitudinally inhomogeneous refractive index.

1.2 ANALYTICAL MODELS

An exact analytical model requires formulation of the real-life problem; calculation of a field component at a given frequency, at any point on or above the earth's surface, caused by a point source on or above the lossy ground, which is characterized by surface impedance boundary condition, in spherical coordinates. The model shall include surface irregularities (rough surface, non-flat terrain, etc.) as well as longitudinal and/or transverse refractivity variations. Unfortunately, this model has not appeared yet, but a model for smooth spherical earth with homogeneous or standard atmosphere (defined in the next sections) has been in use for several decades.

1.2.1 Statement of the Problem

Consider the problem given in Fig. 1.3 and assume wave propagation over the smooth spherical earth with impedance boundary conditions. Further assume homogeneous atmosphere and consider a vertical electric dipole located near the earth's surface as the source. In spherical (r,θ,φ) coordinates the earth's radius is $r = a$, finite conductivity of the earth's surface at $r = a$ is described by the surface impedance Z_s.

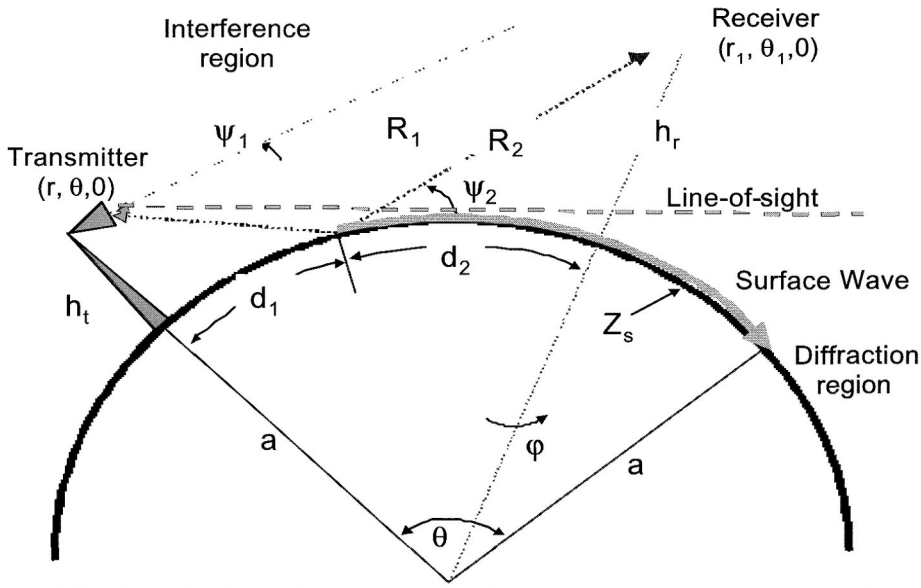

Figure 1.3: *Spherical earth geometry with smooth terrain, in spherical polar coordinates. Also shown are transmitter and receiver heights, as well as path lengths associated with wave processes discussed in 1.2.5. Here, ψ_1 denotes the angle between the direct ray and the tangent to the earth's surface at the ray reflection point.*

Under the assumption of azimuthal symmetry for the proposed problem and $\exp(-j\omega t)$ time dependence the fields of a dipole source located on the polar axis $\theta = 0$ at $r' \geq a$ can then be derived from the radial component $rU(r,\theta)$ of the electric Hertz vector as [3],

$$\vec{E} = \nabla \times \nabla \times (Ur\vec{e}_r) \tag{1.5}$$

$$\vec{H} = -j\omega\varepsilon\nabla \times (Ur\vec{e}_r) \tag{1.6}$$

or in component form [3,4]

$$E_r = -\frac{1}{r\sin\theta}\frac{\partial}{\partial\theta}\sin\theta\frac{\partial U}{\partial\theta} \tag{1.7}$$

$$E_\theta = \frac{1}{r}\frac{\partial^2}{\partial r\partial\theta}(rU) \tag{1.8}$$

$$H_\varphi = j\omega\varepsilon \frac{\partial U}{\partial \theta} \tag{1.9}$$

and

$$E_\varphi = H_\theta = H_r = 0 \tag{1.10}$$

where ε denotes the dielectric constant of the exterior region, $r > a$. The function $U(r,\theta)$ satisfies the homogeneous wave equation

$$(\nabla^2 + k^2)U = 0 \tag{1.11}$$

everywhere in the exterior region except at the source region. Here, $k = \omega\sqrt{\varepsilon\mu}$ is the wavenumber. The boundary conditions are radiation condition for $|r| \to \infty$ and an impedance boundary condition on the earth's surface. The latter can be expressed as

$$\vec{n}\times\vec{E} = Z_s\vec{n}\times(\vec{n}\times\vec{H}) \qquad \text{(on earth's surface)} \tag{1.12}$$

where $\vec{n}$ is the outward unit vector normal to the surface and Z_s denotes ground impedance. For this problem, impedance boundary condition becomes [11]

$$E_\theta = -Z_s H_\varphi,\ Z_s = Z_0\left[\frac{j\omega\varepsilon_0}{\sigma_g + j\omega\varepsilon_g}\right]^{1/2}\left[1 + \frac{j\omega\varepsilon_0}{\sigma_g + j\omega\varepsilon_g}\right]^{1/2} \tag{1.13}$$

where $Z_0 = 120\pi$ is the free-space wave impedance, ε_g and σ_g are the permittivity and conductivity of the ground, respectively. Substituting from (1.8), (1.9), and (1.10) one obtains

$$\frac{1}{r}\frac{\partial}{\partial r}[rU] = -j\omega\varepsilon Z_s U \qquad \text{at } r = a \tag{1.14}$$

1.2.2 Equivalent Earth's Radius Concept

The atmosphere is assumed to be homogeneous in the above formulations. However, in reality, the dielectric constant decreases smoothly and monotonically with increasing height, $h = r\text{-}a$. When this weak radial inhomogeneity is taken into account, (1.7)-(1.9) become [4]

$$E_r = -\frac{1}{r\sin\theta}\frac{\partial}{\partial\theta}\sin\theta\frac{\partial U}{\partial\theta} \tag{1.15}$$

$$E_\theta = \frac{1}{r\varepsilon_r(r)}\frac{\partial}{\partial r}\left(\varepsilon_r(r)r\frac{\partial U}{\partial\theta}\right) \tag{1.16}$$

$$H_{\varphi} = \frac{jk_0\varepsilon_r(r)}{Z_0}\frac{\partial U}{\partial \theta} \tag{1.17}$$

$$\frac{\partial}{\partial r}\frac{1}{\varepsilon_r(h)}\frac{\partial}{\partial r}[\varepsilon_r(h)rU]+\frac{1}{r\sin\theta}\frac{\partial}{\partial \theta}\sin\theta\frac{\partial}{\partial \theta}U+k_0{}^2n^2(h)rU=0 \tag{1.18}$$

$$\frac{1}{r\varepsilon_r(r)}\frac{\partial}{\partial r}[\varepsilon_r(r)rU]=j\omega\varepsilon_r(r)Z_sU \qquad \text{on } r=a \tag{1.19}$$

where $\varepsilon_r(h)=\varepsilon(h)/\varepsilon_0$ is the dielectric constant relative to permittivity ε_0 of the free space and k_0 is the free space wavenumber. It now proves to be convenient to factor out a rapidly varying phase term by introducing an auxiliary quantity $\widetilde{U}$ [4] defined as

$$\widetilde{U} = e^{-jk_ra\theta}\varepsilon_r(h)r\sqrt{\sin\theta}U \tag{1.20}$$

Substituting from (1.20) into (1.18), it can be shown that the wave equation is satisfied and $\widetilde{U}$ can approximately be reduced to the following parabolic form

$$\frac{\partial^2\widetilde{U}}{\partial r^2}+2j\frac{k_0}{a}\frac{\partial\widetilde{U}}{\partial\theta}+k_0^2\left(\frac{\varepsilon_r(h)}{\varepsilon_r(0)}-\frac{a^2}{r^2}\right)\widetilde{U}=0 \tag{1.21}$$

We will introduce a change of variables via

$$\begin{aligned} h &= r-a \\ s &= a\theta \end{aligned} \tag{1.22}$$

Then using the approximate equality

$$1-\frac{a^2}{r^2}\cong\frac{2h}{a} \tag{1.23}$$

(1.21) can be written as

$$\frac{\partial^2\widetilde{U}}{\partial h^2}+2jk_0\frac{\partial\widetilde{U}}{\partial s}+k_0^2\left(\frac{\varepsilon_r(h)-\varepsilon_r(0)}{\varepsilon_r(0)}+\frac{2h}{a}\right)\widetilde{U}=0 \tag{1.24}$$

In order to combine the effect of both earth radius and inhomogeneous atmosphere in one parameter, the equivalent earth radius a_e is defined as

$$\frac{1}{a_e}=\frac{1}{a}+\frac{\varepsilon_r'(0)}{2\varepsilon_r(0)} \qquad \text{where} \quad \varepsilon_r'(0)=\left(\frac{\partial\varepsilon_r}{\partial h}\right)_{h=0} \tag{1.25}$$

and (1.24) becomes

$$\frac{\partial^2 \widetilde{U}}{\partial h^2} + 2jk_0 \frac{\partial \widetilde{U}}{\partial s} + \frac{2k_0^2}{a_e} h(1+g)\widetilde{U} = 0 \tag{1.26}$$

where

$$g = \frac{a_e}{2\varepsilon_r(0)}\left(\frac{\varepsilon_r(h) - \varepsilon_r(0)}{h} - \varepsilon_r'(0)\right) \tag{1.27}$$

If the refractive index of the atmosphere varies linearly with h, then $g=0$ and (1.26) reduces to

$$\frac{\partial^2 \widetilde{U}}{\partial h^2} + 2jk_0 \frac{\partial \widetilde{U}}{\partial s} + \frac{2k_0^2}{a_e} h\widetilde{U} = 0 \tag{1.28}$$

On the other hand, in a homogeneous atmosphere, $\varepsilon_r(h) = \varepsilon_r(0)$ for all h and using (1.24) and (1.26), one then obtains

$$\frac{\partial^2 \widetilde{U}}{\partial h^2} + 2jk_0 \frac{\partial \widetilde{U}}{\partial s} + \frac{2k_0^2}{a} h\widetilde{U} = 0. \tag{1.29}$$

From (1.28) and (1.29) it is clear that propagation in a "linear atmosphere" can equivalently be considered as the propagation over an earth with a homogeneous atmosphere, provided that the earth radius a is modified to be the effective earth radius a_e. Since $\varepsilon_r(0) \approx 1$, (1.24) can be rewritten as

$$\frac{\partial^2 \widetilde{U}}{\partial h^2} + 2jk_0 \frac{\partial \widetilde{U}}{\partial s} + k_0^2\left(\varepsilon_r(h) - 1 + \frac{2h}{a}\right)\widetilde{U} = 0. \tag{1.30}$$

1.2.3 Transformation to Non-Dimensional Quantities

The normalized coordinates for the relevant source height (h) and observation height (h'), which satisfy the inequalities $h'/a << 1$ and $h/a << 1$ are introduced as [3,4]

$$\zeta = \frac{k_0 s}{2m^2}, \qquad \xi = \frac{k_0 h}{m}, \qquad \xi' = \frac{k_0 h'}{m} \qquad q = jm\varepsilon_r(0)\frac{Z_s}{Z_0} \tag{1.31}$$

where

$$m = \left(\frac{k_0 a}{2}\right)^{1/3} \tag{1.32}$$

If an attenuation function is defined as

$$V(\xi, \xi', \zeta, q) = 2\sqrt{\pi\zeta}\, e^{j\pi/4} F(\xi, \zeta) \tag{1.33}$$

the quantity $\widetilde{U}$ can be expressed in the form of V as

$$\widetilde{U} = \sqrt{\frac{a}{s}} V \qquad \Rightarrow \qquad \widetilde{U} = \sqrt{\frac{m}{\zeta}} V \tag{1.34}$$

and eq. (1.30) can be approximated in "earth-flattening" non-dimensional rectangular (ξ, ζ) coordinates as

$$\left[\frac{\partial^2}{\partial \xi^2} + j \frac{\partial}{\partial \zeta} + p(\xi) \right] F = 0 \tag{1.35}$$

where the equivalent permittivity function $p(\xi)$ is given by

$$p(\xi) = \xi + m^2 \left[\varepsilon_r(\xi) - 1 + \frac{2h}{a} \right] \tag{1.36}$$

The boundary condition at (1.19) is expressed as

$$\frac{\partial F(\xi, \zeta)}{\partial \xi} + qF(\xi, \zeta) = 0 \qquad \text{for } (\xi = 0) \tag{1.37}$$

for the transformed rectangular co-ordinates.

1.2.4 Exact Spectral Solution

Consider the Green's function problem [11] corresponding to (1.35) - (1.36)

$$\left[\frac{\partial^2}{\partial \xi^2} + j \frac{\partial}{\partial \zeta} + p(\xi) \right] F(\xi; z) = -\delta(\zeta) \delta(\xi - \xi') \tag{1.38}$$

where the source location is $\zeta = 0$ (s, $\theta = 0$) and $\xi' = k_0 h' / m$, with h' being the height of the source above ground and it is assumed that $h' << a$. This equation is Fourier transformed in ζ-domain using the transform pair

$$F(\xi, \xi' \zeta) = \frac{-1}{j2\pi} \int_{\beta=-\infty}^{\infty} e^{j\beta\zeta} g_\xi(\xi, \xi'; \beta) d\beta$$

$$g_\xi(\xi, \xi'; \beta) = \int_{\zeta=-\infty}^{\infty} F(\xi, \xi'; \zeta) e^{-j\beta\zeta} d\zeta \tag{1.39}$$

and one obtains a one-dimensional spectral Green's function problem in the ξ-domain as

$$\left[\frac{d^2}{d\xi^2} + (p(\xi) - \beta) \right] g_\xi(\xi, \xi'; \beta) = -\delta(\xi - \xi') \tag{1.40}$$

The corresponding impedance boundary condition can be obtained from (1.37) by replacing F with g_ξ and a radiation condition should be imposed for $\xi \to \infty$. The solution of (1.40) can be written as

$$g_\xi(\xi,\xi';\beta) = \frac{[f_2(\xi_<,\beta) + R_0 f_1(\xi_<,\beta)]f_1(\xi_>,\beta)}{W[f_1,f_2]} \tag{1.41}$$

where $\xi_<$ and $\xi_>$ denote the smaller or larger values of ξ and ξ', respectively. The Wronskian is given by

$$W[f_1,f_2] = f_1 f_2' - f_1' f_2, \qquad f' \equiv \frac{d}{d\beta} f \tag{1.42}$$

and the reflection coefficient R_0 by

$$R_0 = -\frac{f_2'(0,\beta) + q f_2(0,\beta)}{f_1'(0,\beta) + q f_1'(0,\beta)} \tag{1.43}$$

In these equations f_1 and f_2 denote two linearly independent progressing (traveling) wave solutions of the source-free equation corresponding to (1.40) which are employed in proper combination in order to ensure that all boundary conditions are satisfied. Clearly, closed-form solutions of the source free equation can only be obtained for a few special permittivity profiles. Then the spectral integral for $F(\xi,\zeta)$ in (1.38) can be evaluated using residue calculations and/or asymptotic saddle point techniques. Expanding the resonant denominator W in (1.41) by power series and evaluating the terms of these series asymptotically at the saddle points yields the ray representation, while evaluating the spectral integral in terms of the residues yields the modal representations.

1.2.5 Ray Asymptotics: Norton Formulation

In the standard atmosphere, three terms are obtained via ray-asymptotic evaluation of the spectral integral in eq. (1.39): the direct wave from the source to the observer, the ground-reflected wave, and the surface wave, with the sum of the first two contributions also referred to as the space wave. In his classic paper [8], Norton gives expressions for the vertical and tangential electric field components in the earth-flattening approximation. The problem has been addressed in [29], where the three components of the ground wave are expressed in cylindrical co-ordinates [11]. The exact solution to the problem of an antenna above a spherical finitely conducting earth can be set up in terms of an infinite series of spherical harmonics with coefficients containing 12 Bessel functions [11,29]. The convergence of these series is extremely slow, and for commonly used radio frequencies, as many as 10^3 to 10^8 terms are necessary for the calculation of the dominant contribution [11,29]. On the other hand the space-wave component (sum of direct and ground-reflected wave) can easily be constructed in spherical co-ordinates directly from the geometrical relations in Fig. 1.3 [11]. The space-wave components can be expressed as

$$E_{ver} = E_0\left[\cos^2\psi_1 + D\Gamma_v \frac{R_1}{R_2}\cos^2\psi_2\, e^{jk_0\Delta R}\right] \tag{1.44}$$

$$E_{\tan} = E_0\left[\cos\psi_1 \sin\psi_1 + D\Gamma_v \frac{R_1}{R_2}\cos\psi_2 \sin\psi_2\, e^{jk_0\Delta R}\right] \tag{1.45}$$

where

$$E_0 = ik_0 Z_0 M_0 \frac{e^{jk_0 R_1}}{4\pi R_1} = -j30k_0 M_0 \frac{e^{jk_0 R_1}}{R_1} \tag{1.46}$$

is the direct (free space) electric field strength at an arc-distance d generated by an electric dipole with moment $M_0 = I\,dl$. The distances R_1 and $R_2 \equiv R_1 + \Delta R$ (incident plus reflected path length) are given by

$$R_1 = \left[(a_e + h_1)^2 + (a_e + h_2)^2 - 2(a_e + h_1)(a_e + h_2)\cos\frac{d}{a_e}\right]^{1/2} \tag{1.47}$$

$$\Delta R = R_2 - R_1 = \frac{2h_1 h_2}{d}(1 - S_1^{\,2})(1 - S_2^{\,2}) \tag{1.48}$$

where

$$S_1 = \frac{d_1}{\sqrt{2a_e h_1}}, \qquad S_2 = \frac{d_2}{\sqrt{2a_e h_2}} \tag{1.49}$$

$$d_1 = \frac{d}{2} + \rho\cos\left(\frac{\psi + \pi}{3}\right), \quad d_2 = d - d_1, \quad \psi = \cos^{-1}\left[\frac{2a_e}{\rho^3}(h_2 - h_1)d\right] \tag{1.50}$$

$$\rho = \frac{2}{\sqrt{3}}\left[a_e(h_1 + h_2) + \frac{d^2}{4}\right]^{1/2} \tag{1.51}$$

$$h_1 = h_t\,, \quad h_2 = h_r \text{ for } h_t < h_r;\; h_1 = h_r\,, \quad h_2 = h_t \text{ for } h_t > h_r \tag{1.52}$$

In the above, d is the arc distance between the transmitter and receiver, d_1 and d_2 are the arc distances from the transmitter and receiver to the reflection point on the ground, a and a_e are the earth's radius and effective radius, and h_t and h_r are the transmitter and receiver heights, respectively. In (1.44) and (1.45), the ray field reflection coefficient at the specular reflection point on the surface is

$$\Gamma_v = -\frac{\bar{\varepsilon}_g \sin\psi_2 - \sqrt{(\bar{\varepsilon}_g - \cos^2\psi_2)}}{\bar{\varepsilon}_g \sin\psi_2 + \sqrt{(\bar{\varepsilon}_g - \cos^2\psi_2)}} \tag{1.53}$$

with the angular coordinates given by

$$\psi_2 = \tan^{-1}\left\{\left(\frac{h_1+h_2}{d}\right)\left(\frac{(1-S_2{}^2)+T^2(1-S_1{}^2)}{1+T^2}\right)\right\} \tag{1.54}$$

$$\psi_1 = \begin{cases} \cos^{-1}\left[\dfrac{-(h_2+a_e)^2+(h_1+a_e)^2+R_1{}^2}{2(h_1+a_e)R_1}\right]-\dfrac{\pi}{2}; & h_t < h_r \\ \cos^{-1}\left[\dfrac{-(h_1+a_e)^2+(h_2+a_e)^2+R_1{}^2}{2(h_2+a_e)R_1}\right]-\dfrac{\pi}{2}; & h_t > h_r \end{cases} \tag{1.55}$$

Finally, in (1.44), D is the ray divergence factor at the reflection point, which accounts for the curvature effects of the spherical earth and is given as

$$D = \left[1+\frac{4S_1S_2{}^2T}{S_1(1-S_2{}^2)(1+T)}\right]^{-1/2}, \qquad T=\sqrt{\frac{h_1}{h_2}}. \tag{1.56}$$

1.2.6 Modal Residue Series: Wait Formulation

Calculating the residues of $g_\xi(\xi,\xi';\beta)$ in the spectral integral (1.39), the function F may be expressed in terms of height gain functions. In this formulation, the vertical (radial) component of electric field for the configuration in Fig. 1.3 is obtained as

$$E_{ver.} = E_0 V(\xi,\xi',\zeta,q) \tag{1.57}$$

where E_0 is given in (1.48) and attenuation function, V, in (1.46) is expressed as

$$V(\xi,\xi',\zeta,q) = e^{j\pi/4}2\sqrt{\pi\zeta}\sum_{s=1}^{\infty}e^{j\beta_s\zeta}\frac{d\beta_s}{dq}\frac{W(\beta_s-\xi)}{W(\beta_s)}\frac{W(\beta_s-\xi')}{W(\beta_s)} \tag{1.58}$$

Here β_s are the spectral poles of $g_x(x,x';\beta)$, and

$$\frac{W(\beta_s-\xi)}{W(\beta_s)} \tag{1.59}$$

is the "height-gain" function. All parameters are defined as in (1.31) and (1.32). For the standard atmosphere model including the effects of the earth's curvature (i.e., linearly increasing equivalent vertical profile), the transverse mode functions are the well-known solutions of the Airy equation [30],

$$W(\beta) = \sqrt{\pi}\ [Bi(\beta) - jAi(\beta)] \tag{1.60}$$

which satisfies the impedance boundary condition on $x = 0$,

$$\left[\frac{d}{d\beta}W(\beta)-qW(\beta)\right]_{\beta=\beta_s}=0 \tag{1.61}$$

and the radiation condition at $x \to \infty$. Now, the wave phenomenology is modeled via transverse (x-domain) oscillatory modal fields, which progress with fixed wavenumber β_s along z. Only the radial component of the electric field excited by a vertically polarized short dipole is given because the tangential component of the field is negligible. The height gain functions are convenient to parameterize the effects of both transmit and receive antenna heights with respect to path loss variations.

1.3 NUMERICAL MODELS

EM waves excited from a vertical electric dipole (VED) located over the ground in 2D Cartesian co-ordinates requires us to study a TM_z problem with the field components E_x, H_y and E_z, where x and z are chosen as the transverse (height) and longitudinal (range) coordinates, respectively (see Fig. 1.4). For a horizontal electric dipole (HED) located over the ground, a TE_z problem with the field components H_x, E_y and H_z, has to be considered. If the operating frequency is at HF region, horizontally polarized waves are heavily attenuated; therefore vertically polarized antennas are required to generate efficient ground wave propagation. For both VED and HED excitations, the propagation region is a semi-infinite region that extends from $x = 0$ (bottom) to $x \to \infty$ (top), and from $z \to -\infty$ (left) to $z \to \infty$ (right).

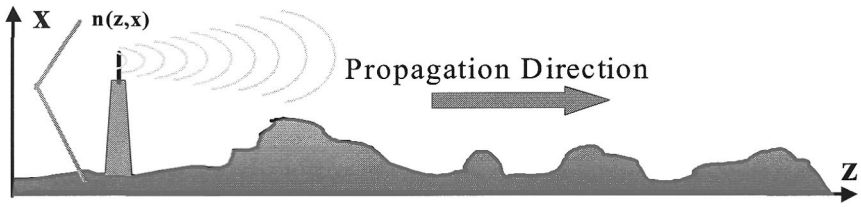

Figure 1.4: *The 2D propagation space for numerical simulators*

Numerical ground wave propagation models included here are SSPE, TDWP and TLM-WP and are basically the solutions of parabolic type 2D wave equation and Maxwell's equations in 2D, respectively.

1.3.1 Split-Step Parabolic Equation (SSPE) Propagator

The Fourier Split Step algorithm used to solve parabolic type equations is common and popular for the modeling of electromagnetic wave propagation in the troposphere. Although there are other propagation models capable of accounting for horizontal refractive gradients, they are restricted to simplistic refractive conditions, lower frequencies, and/or certain regions of space. Leontovich and Fock [4, Chapter 11] are pioneers who described the use of parabolic equation (PE) for electromagnetic wave propagation in a vertically inhomogeneous medium. However, this approach has become famous after the introduction of the Fourier Split-Step algorithm by Tappert [31,32]. Tappert's aim was to describe acoustic wave propagation in the ocean, but his approach then applied to electromagnetic wave propagation in troposphere.

The standard parabolic wave equation is given as

$$\frac{\partial^2 u}{\partial x^2} + 2jk_0 \frac{\partial u}{\partial z} + k_0^2 (n^2 - 1)u = 0 \tag{1.62}$$

where u denotes the wave amplitude and x and z stand for transverse (i.e., height above ground) and longitudinal (i.e., the direction of propagation) coordinates, respectively. For VED (HED) $u(z,x)$ is related to magnetic field component (electric field component) that is perpendicular to the computation plane. In other words, in Cartesian coordinates

$$H_y(z,x) \equiv u(z,x) \qquad (VED)$$
$$E_y(z,x) \equiv u(z,x) \qquad (HED)$$

Equation (1.62) may be solved in the transverse wavenumber (k_x) domain at each range step, Δz, where the refractive index can be treated as constant. Applying a Fourier transform, solving the reduced equation there and then transforming back to transverse (x) spatial domain, one obtains classical SSPE form

$$u(z,x) = \exp\left[j\frac{k_0}{2}(n^2 - 1)\Delta z \right] F^{-1}\left[\exp\left[-j\frac{k_x^{\,2}\Delta z}{2k_0} \right] F\{u(z_0,x)\} \right] \tag{1.63}$$

This equation can be used to propagate a given initial field distribution $u(z_0,x)$ along z to $u(z,x)$ in steps of Δz. To speed up the procedure Fourier transforms are implemented via the fast Fourier transform (FFT) algorithm. Since PE is an initial value problem, an initial transverse field distribution, $u(z_0,x)$ is injected at an initial range, z_0, (e.g., $z_0 = 0$) then it is longitudinally propagated through a medium defined by its refractive index profile, $n(z,x)$ and the transverse field profile $u(z_0+\Delta z,x)$, at the next range step, is obtained.

The classical SSPE flow chart is given in Fig. 1.5 and implementation steps are listed in Section 1.6.2 of Part I. The program starts with the user supplied initial vertical scalar field profile, some parameters (such as frequency, maximum height, first range, last range, range increment, etc.) and vertical refractivity profile that may also be range-dependent. By sequential operations accessing the x and k_x domains via FFT and inverse FFT, respectively, one may obtain the transverse field profile at any range. In 2D rectangular coordinates, the earth's curvature is included by modifying the refractivity profile. Extra terms may also be added to model various super or sub-refraction propagation cases. Each run contains one forward and one backward FFTs. After each run, the program checks whether the last range supplied by the user has been reached or not. If not, the loop in Fig. 1.5 continues by replacing calculated vertical field profile as the new input field profile at each range, and when last range is reached, output is written and program terminates.

Boundary conditions must be implemented in SSPE algorithm since it is the solution of an initial value problem. If the ground is assumed to be a perfect electrical conductor,

Dirichlet and Neumann BCs are needed for VED and HED, respectively. Sine (cosine) Fourier transformation automatically satisfies Dirichlet (Neumann) BC. Another way of handling these BCs is as shown in Fig. 1.6. Here, the 2D propagation space that extends from $x = 0$ to $x = X_{max}$ vertically and from $z = z_0$ to $z \rightarrow \infty$ horizontally, and initial vertical field profile of SSPE wave propagator at range $z = z_0$ is shown on the left. The Dirichlet (Neumann) BC at the surface is satisfied by extending vertical profile odd (even) symmetric with respect to $x = 0$ axis (in the middle). After one SSPE run the next vertical field profile $u(z_0+\Delta z,x)$ at the next range step $z = z_0+\Delta z$ is obtained (on the right). On the other hand, Cauchy (impedance) BC is needed mostly at HF and lower VHF regions where the ground cannot be accepted as PEC because of the dominant surface wave propagation. However it is difficult to model impedance boundary condition and needs a lot of computation. Recently, discrete mixed Fourier transformation (DMFT) has been introduced [15] to handle impedance BC in SSPE.

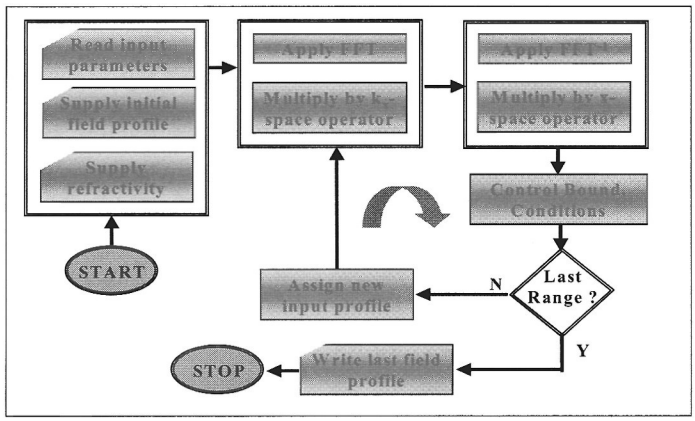

Figure 1.5: *Flow chart of SSPE routine*

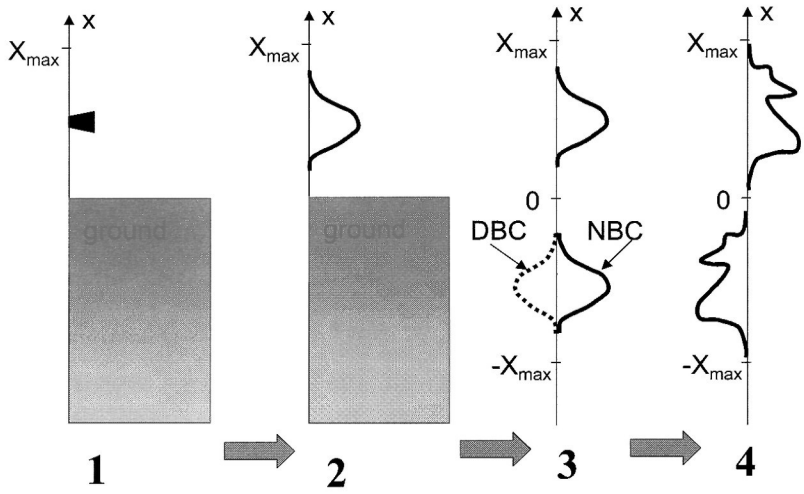

Figure 1.6: *Satisfaction of Dirichlet or Neumann BC in SSPE*

1.3.1.1 Classical SSPE Algorithm

The classical SSPE algorithm is a few-line code as a main routine. The initial vertical field profile array is fed into an FFT routine, multiplied by an exponent term in transverse wavenumber domain, then a inverse FFT, followed by another complex exponent multiplication, is applied. Here, this classical SSPE code, written in FORTRAN programming language, is listed together with explanations. Only the necessary code parts are listed. The variable declaration, array and file definitions, FFT sub-routine, etc., are not included.

The algorithm first requires the user to input initial parameters:

```
WRITE(*,*) 'LAST RANGE, Z2=? (km)'                READ(*,*) Z2
WRITE(*,*) "RANGE STEP SIZE , DELZ=? (km)'        READ(*,*) DELZ
WRITE(*,*) 'SOURCE HEIGHT=? (m)'                  READ(*,*)  X_SOURCE
WRITE(*,*) "OBSERVATION HEIGHT=? (m)'             READ(*,*) Y_OBS
WRITE(*,*) 'BEAMWIDTH=[DEGREE]?'                  READ(*,*) BW
BW=BW*PI/180.
```

Then discrete transverse wave number ($p=k_x$) points are calculated, where N is the FFT size and DELX is the height step size, respectively.

```
DO L=1,N
   KX(L)=-1/(2*DELX)+(L-1)/(N*DELX)
END DO
```

In this sample algorithm, vertical source profile (i.e., antenna pattern) is chosen as a Gaussian function. The normalized Gaussian antenna pattern is

$$f(p) = e^{-p^2 w^2/4}, \qquad w = \frac{\sqrt{2\ln 2}}{k_0 \sin(BW/2)}$$

where BW is the 3 dB beam-width, and k_0 is the free-space wavenumber. The antenna pattern at z = 0, in transverse wavenumber domain is directly obtained from the function $f(p)$ as

$$\varphi(0,p) = f(p)e^{-jpx_0} - f(-p)e^{jpx_0}$$

to satisfy the Dirichlet boundary condition. This corresponds to

```
IF(L.GT.N/2) THEN
    CFIELD(L)=EXP(-(2*PI*KX(L)*W/2)**2)*EXP(-J* KX(L)*SOURCE)
ELSE
    CFIELD(L)=-EXP(-(2*PI*KX(N-L+1)*W/2)**2)*EXP(J*KX(L)*SOURCE)
ENDIF
```

in the algorithm, where CFIELD is the complex field array. The spatial source distribution at the starting range is obtained by applying an inverse FFT to the function $\varphi(0,p)$. Any type of transverse and/or longitudinal refractive index profile can be

implemented in the algorithm. For example, a linearly decreasing refractive index height profile is

```
DO L=1,N
  IF(X(L).GE.0.0) THEN
     REFR(L)=1.00060009+A0*X(L)
  ELSE
     REFR(L)=1.00060009-A0*X(L)
  ENDIF
END DO
```

where X(L) and REFR(L) are height and refractive index arrays, respectively. Here, A0 denotes the height gradient of the refractive index. If the refractive index has range dependence, its definition should be renewed at each range step. In this sample algorithm, the pre-defined source function is propagated at each range step based on the flowchart given in Fig. 1.5. The transverse wavenumber (*p-space*) complex operator is computed as

```
DO L=1,N
    CPSPACE(L)=CEXP(-J*DELZ*(KX(L)*2*PI)**2/(2*K0))
END DO
```

while complex *z-space* operator is computed as

```
DO L=1,N
    CZSPACE(L)= CEXP(J*DELZ*K0*(REFR(L)-1)/2)
END DO
```

for all height points. The same sub-routine is used for both FFT (Flag 1) and inverse FFT (Flag 0) calculations. The main routine is then written as

```
DO Z=Z1,Z2,DELZ
   CALL FFT(CFIELD, N, 1)                    ! Apply FFT
   DO L=1,N
      CFIELD(L)=CFIELD(L)*CPSPACE(L)
   END DO
   CALL FFT(CFIELD, N, 0)                    ! Apply inverse FFT
   DO L=1,N
      CFIELD(L)=CFIELD(L)* CZSPACE(L)
   END DO
END DO
```

SSPE is a reliable technique for the electromagnetic propagation problems, where back-scattered fields are not required and parabolic (paraxial) approximation is acceptable. Parabolic approximation is used for nearly horizontal propagation directions [31,33 - 35]. In other words, it is used in problems where *u(z,x)* varies slowly with range. That also suggests that *n(z,x)* should vary smoothly with *z* as well as with *x*. The parabolic equation approximation affects the accuracy of the calculations, so it is required to analyze the order of error. The parabolic wave equation obtained for tropospheric propagation is exactly analogous to that obtained for acoustic

propagation in the ocean; therefore the conclusions of acoustic parabolic equation investigations are instructive.

In certain classes of problems the parabolic approximation results in significant modal phase velocity errors for propagation in directions with angles more than ≈15° from the horizontal axis (range). These errors become evident in problems where an oceanic duct or shallow region gives rise to a coherent sum of several trapped modes propagating at relatively large angles. It is possible to correct these errors using the wide-angle approximation, which is explained in [36,37]. On the other hand, atmospheric refractive index gradients that trap angles larger than ≈1° are rare and a relatively large gradient in troposphere corresponding to a strong duct is at about $|\partial n/\partial x| \approx 10^{-6}$ m^{-1} (i.e. smaller than $\approx 3\times10^{-4}$ m^{-1}, which is given in [36] as a typical example case). Therefore, the investigation of most electromagnetic problems with parabolic approximation is adequate and there is no need for the wide-angle propagation approximation. The wide-angle algorithm is required only for the problem geometries (i.e., high antennas at short ranges or the non-flat surfaces, which consist large slopes resulting in wide-spread scattering of the propagating wave) where angles greater than 15° are of interest.

1.3.1.2 Calibration Against Analytical Exact Solution

In order to show the accuracy of the SSPE algorithm, propagation over flat earth with a linearly decreasing vertical refractivity profile is considered. This problem has analytical exact solutions in terms of Airy functions, when the refractive index is defined as

$$n^2(x) = 1 - a_0 x \tag{1.64}$$

Here a_0 is a positive constant. In such a non-homogeneous environment scalar function u*(x,z)* satisfies the wave equation

$$\frac{\partial^2 u}{\partial x^2} + \frac{\partial^2 u}{\partial z^2} + k_0^2 n^2(x) u = 0 \tag{1.65}$$

subject to homogeneous boundary condition at $x = 0$

$$\alpha_1 \left.\frac{\partial u}{\partial x}\right|_{x=0} + \alpha_2 u(x=0) = 0, \tag{1.66}$$

where α_1, α_2 are constants, and $\alpha_{1,2} = 0$ results in Dirichlet and Neumann conditions respectively. The radiation boundary condition is

$$\begin{aligned} u(x,z)\big|_{x\to\infty} &\to 0 \\ u(x,z)\big|_{z\to\mp\infty} &\to 0 \end{aligned} \tag{1.67}$$

Recalling that the time dependence is taken as $e^{-j\omega t}$, the modal series solution can be expressed as

$$u(x,z)=\sum_{q=0}^{\infty} C_{0q}\psi_q(x)e^{j\beta_q z} \tag{1.68}$$

where β_q is the longitudinal propagation constant k_z. for the related mode represented by index q. The new function $\psi_q(x)$ satisfies the one-dimensional wave equation

$$\left[\frac{d^2}{dx^2}+k_0^2n^2(x)-\beta_q^2\right]\psi_q(x)=0 \tag{1.69}$$

In order to solve this equation new variables are defined as

$$k_0^2n^2(x)-\beta_q^2=K_1x+K_2, \qquad \rho=-K_1^{-2/3}(K_1x+K_2) \tag{1.70}$$

and the wave equation becomes an Airy equation

$$\left[\frac{d^2}{d\rho^2}-\rho\right]\psi_q(\rho)=0 \tag{1.71}$$

The solution of this equation with BCs given in (1.66) and (1.67) is constructed in terms of modes that are represented by the first kind of Airy function $A_i(\rho)$, with ρ being real.

$$\psi_q(\rho)=C_{0q}A_i(\rho) \tag{1.72}$$

where C_{0q} is the normalization constant defined as

$$C_{0q}=\left[\int_0^{\infty}A_i^2(\rho)d\rho\right]^{-1/2} \tag{1.73}$$

If $n^2(x)=1-a_0x$ is used in the one-dimensional wave equation

$$K_1=-a_0k_0^2 \quad \text{and} \quad K_2=k_0^2-\beta_q^2 \tag{1.74}$$

then

$$\rho=(a_0k_0^2)^{1/3}x-(a_0k_0^2)^{-2/3}(k_0^2-\beta_q^2) \tag{1.75}$$

This equation at $x = 0$ is denoted as σ_q, q representing the mode number. The condition at the surface is then reduced to

$$A_i'(-\sigma_q)+\alpha A_i(-\sigma_q)=0 \tag{1.76a}$$

$$A_i(-\sigma_q)=0 \tag{1.76b}$$

$$A_i'(-\sigma_q)=0 \tag{1.76c}$$

for Cauchy-, Dirichlet-, and Neuman-type BCs, respectively. Here, the prime denotes the derivative with respect to vertical coordinate. The longitudinal propagation constant is found as for each mode

$$\beta_q=\pm\left[k_0^2-\sigma_q(a_0k_0^2)^{2/3}\right]^{1/2} \tag{1.77a}$$

and modes are trapped between the surface and their modal caustics determined from

$$X_{cq}=-\sigma_q\left[a_0k_0^2\right]^{-1/3} \tag{1.78b}$$

Finally, the exact modal solution of Airytype wave equation is then found to be

$$u(x,z)=\sum_{q=1}^{N}C_{0q}A_i((a_0k_0^2)^{1/3}x-\sigma_q)e^{j\beta_q z} \tag{1.79}$$

The first and second kind of Airy functions Ai(.) and Bi(.) are real for real arguments. Their variations are pictured in Fig. 1.7. They both have standing wave character when the arguments are negative. While Ai(.) decays exponentially, Bi(.) blows up for positive arguments.

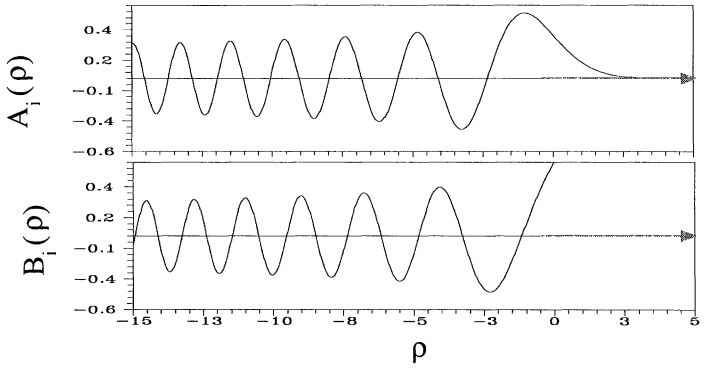

Figure 1.7: *First and second kind of Airy functions for real arguments*

In order to validate the SSPE algorithm, the data computed with (1.79) for the chosen parameters are compared with SSPE solutions, as is seen in Fig. 1.8. Here, $n^2(x)=1-a_0x$ and $a_0=4\times10^{-8}$, which corresponds to the refractive index of standard atmosphere (excluding the effect of earth's radius), causing a surface duct that traps the wave. The ground is assumed to be PEC, satisfying the Dirichlet boundary condition and $k_0 = 2\pi$. First, (1.79) is computed with the first ten modes at z

= 0 km between x = 0 m and x = 2000 m at 512 different height points, and the result is used in SSPE algorithm as the initial height variation of the scalar function, $u(x,z)$. Then height variation of the function at four different ranges, (z = 25 km, z = 50 km, z = 75 km and z = 100 km) is calculated via SSPE and plotted in Fig. 1.8. The results of exact modal solutions computed via (1.79) at the same ranges and heights are also plotted. Perfect agreement between the exact analytical solution and SSPE, which is a semi-analytic-numerical method, is observed in the figure.

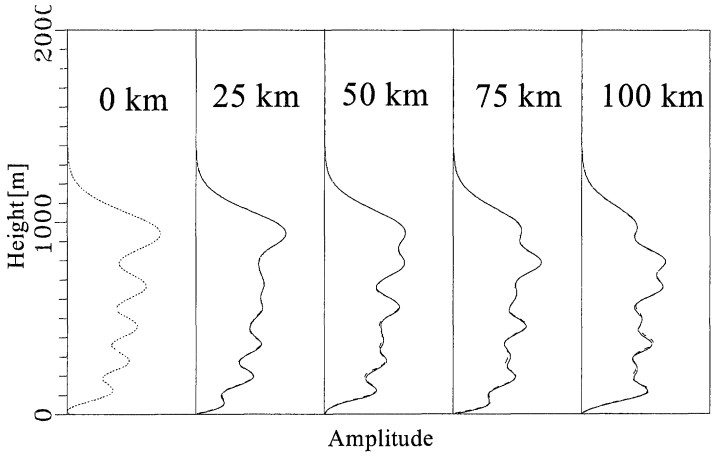

Figure 1.8: *Field vs. height computed with exact analytical solution and SSPE algorithm at different ranges. The height variation at z = 0 is calculated numerically with exact analytical solution and used in SSPE as the initial height variation of the scalar function.*

Modes given in (1.79) are the building blocks (i.e., eigenfunctions) of the geometry (they are orthonormal to each other and have unit energy); therefore, any initial transverse source profile can be represented by superposing them via the proper modal excitation coefficients. Modal excitation coefficients are determined from the completeness relation. Any vertical profile (e.g., a Gaussian field distribution) can be chosen and represented by a modal series. The number of modes can be determined numerically by trial and error. Then, this profile may be used as an input profile of the SSPE program, and results at any range can be obtained both analytically and numerically. This is illustrated in the following example.

Suppose a strongly surface trapping duct, which is specified by (1.64) with a_0 equal to -4×10^{-5}. In this case refractive index at the surface is "1" but reduces to, for example, "0.2" at 20 km height. Frequency is specified as 300 MHz. The source is located 250 m above the ground and has a vertical extend from 100 m to 400 m. This vertical profile is built with the first 100 normal modes, NM (eigenfunctions). Excitation coefficients are between 10^{-4} and 10^{-2} for the first 11 NMs, between 0.1 and 2.23 for NMs 12 - 60, and between 10^{-4} and 10^{-6} for the rest of 40 NMs. Typical comparisons are given in Fig. 1.9 and Fig. 1.10.

In Fig. 1.9, horizontal field profile at 100 m constant height is plotted. Solid and dashed lines correspond to exact analytical and numerical SSPE results, respectively. In Fig. 1.10, vertical field profiles at three ranges (at z = 0 km, 12 km, and 15 km), obtained

with both methods are plotted. Very good agreement is clearly observed, even for the highly oscillatory nature of the field profiles, in the figure.

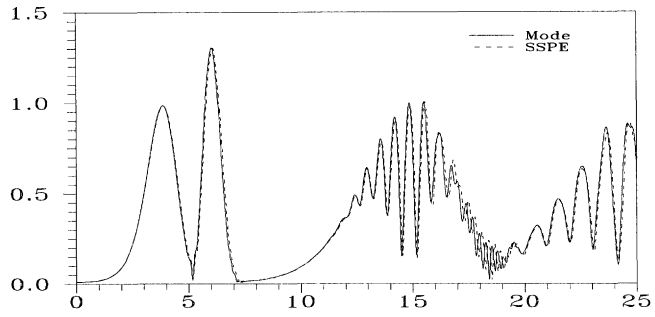

Figure 1.9: Field strength vs. range at a fixed height of 100 m.

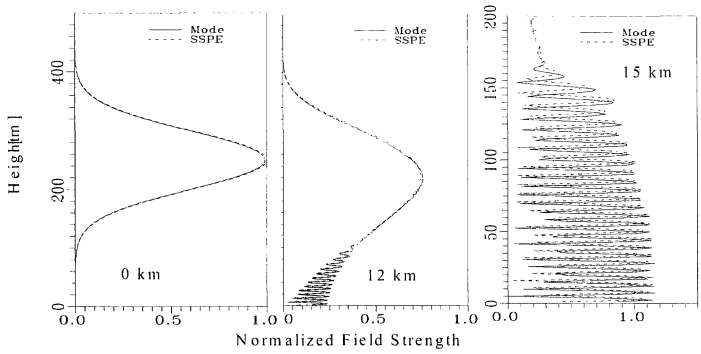

Figure 1.10: Field strength vs. height at z = 0 km, 12 km, and 15 km

Again, perfect agreement obtained between the two methods is clearly observed in both figures.

1.3.1.3 Staircase Terrain Modeling

Longitudinally non-flat terrain can be incorporated into the SSPE algorithm via several different mathematical approaches and it is possible for the user to choose the appropriate one for his/her problem. Here, only the staircase approximation is taken into account. Staircase terrain modeling is simpler, in which slope values are not required (as in the other approximations); only the terrain height for each range is needed. On each segment of constant height, the field is propagated in the usual way for staircase terrain, applying necessary boundary condition at the ground. When terrain height changes, corner diffraction is ignored and the field is simply set to zero on vertical terrain facets. Since the computation height is not changed due to the terrain, there is no need to modify refractive index; therefore it is also easy to implement the staircase terrain modeling into the SSPE algorithm. One just needs to take into account that ground does not support propagation under the constant height for each segment [14]. Although staircase terrain cannot model the terrain as smooth

as it must be, comparisons show that the results are quite satisfactory [38]. A typical non-flat terrain profile and its discrete staircase representation is pictured in Fig. 1.11. The smaller the range and height step sizes (Δz and Δx, respectively) the better the approximation in discrete terrain profile.

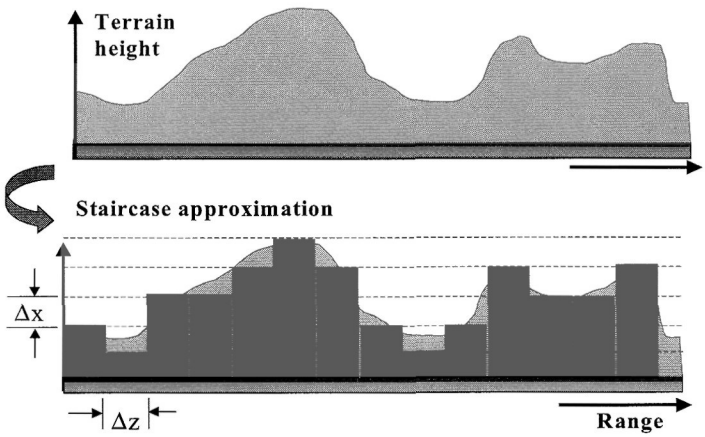

Figure 1.11: *The difference between terrain and its staircase approximation*

In SSPE, terrain effects are included as follows:

- A terrain file contains height vs. range that represents non-flat terrain in the chosen scenario. Zero height corresponds to flat earth's surface.
- A complex array contains field values at discrete height points from the surface (zero height) to maximum height of interest.

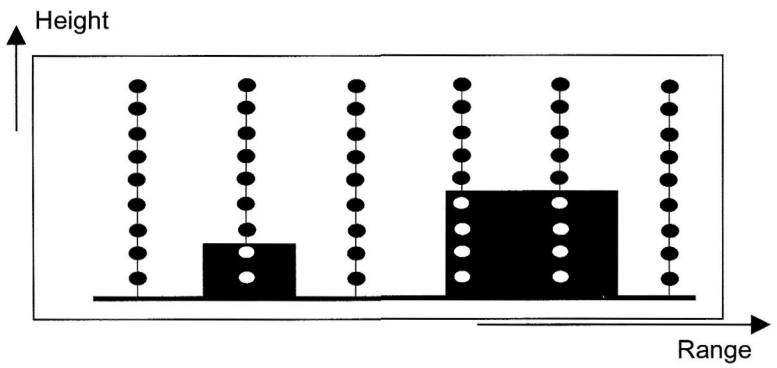

Figure 1.12: *Non-flat terrain implementation in SSPE (black circles are the field values at different height points.; white circles are the ones that are forced to be zero since they are inside the non-flat terrain)*

- Computed vertical field profile at the current range is used as the initial field profile of the next range for next SSPE iteration.

- While propagating step by step the terrain file is checked continuously and height of the terrain at the range of computation is read and array elements (vertical field values below the terrain height), which fall below terrain height at that range are set to zero. This is illustrated in Fig. 1.12.

1.3.2 Time-Domain Wave Propagators (TDWP, TLMWP)

The difficulty of analyzing ground-wave propagation via time-domain (TD) techniques is the necessity of observing the fields towards the extended regions in range, which is impossible for the conventional FDTD [39] or TLM [40] techniques. Although it is possible to use larger computation spaces with higher computer memories, the desired propagation region is always much larger than available FDTD and TLM spaces (see Fig. 1.13).

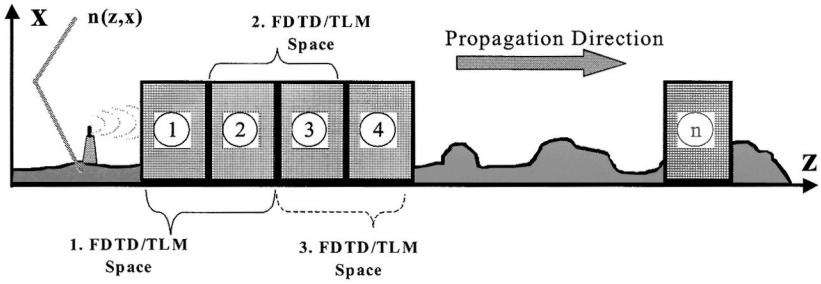

Figure 1.13: *The 2D propagation space, sliding FDTD/TLM windows*

This is overcome by tracing the propagation region with a dynamic sliding window (the FDTD/TLM space). In both TDWP and TLM-WP, the computation space has to be terminated by absorbing boundary blocks (here perfectly matched layer, PML is used) at the left, right, and top of the window. This is pictured in Fig. 1.14 with both TLM and FDTD unit cells. A one-cell transition is used to match FDTD field components to the TLM voltage pulses in order to use the same FDTD-based PML routine in both propagators.

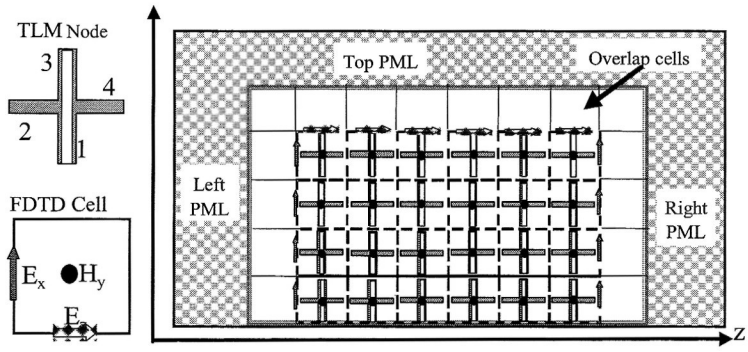

Figure 1.14: *TLM, FDTD cells, the sliding window, and PML blocks*

The related FDTD iterative equations in TDWP are

$$E_x^n(i,k) = \frac{\varepsilon}{\varepsilon + \sigma\Delta t} E_x^{n-1}(i,k) - \frac{\Delta t}{(\varepsilon + \sigma\Delta t)\Delta z}\left[H_y^{n-1/2}(i,k) - H_y^{n-1/2}(i,k-1)\right] \quad (1.80)$$

$$E_z^n(i,k) = \frac{\varepsilon}{\varepsilon + \sigma\Delta t} E_z^{n-1}(i,k) + \frac{\Delta t}{(\varepsilon + \sigma\Delta t)\Delta x}\left[H_y^{n-1/2}(i,k) - H_y^{n-1/2}(i-1,k)\right] \quad (1.81)$$

$$H_y^{n+1/2}(i,k) = H_y^{n-1/2}(i,k) - \frac{\Delta t}{\mu_0 \Delta z}\left[E_x^{n-1}(i,k+1) - E_x^{n-1}(i,k)\right] + \frac{\Delta t}{\mu_0 \Delta x}\left[E_z^{n-1}(i+1,k) - E_z^{n-1}(i,k)\right] \quad (1.82)$$

where ε [F/m], σ [S/m] and μ_0 [H/m] are the permittivity, conductivity and permeability of the propagation medium, respectively. Here, *i* and *k* are the cell numbers in the *x* and z coordinates, respectively, and n tags the time step. FDTD electric field components are calculated at discrete time instants Δt, $2\Delta t$, $3\Delta t$, .., $n\Delta t$, and the magnetic field components are calculated at $\Delta t/2$, $3\Delta t/2$, $5\Delta t/2$, .., $(n+1/2)\Delta t$, in cubical Yee cells [22] with cell sizes Δx, Δy, Δz.

The corresponding TLM components I_y, V_x and V_z are determined from Thevenin equivalence of the series node [23]

$$H_y = \frac{I_y}{\Delta \ell}; \quad E_x = -\frac{V_x}{\Delta \ell}; E_z = -\frac{V_z}{\Delta \ell} \quad (1.83)$$

as

$$I_y = 2\frac{V_1^i - V_2^i - V_3^i + V_4^i + V_5^i}{\hat{Z} Z_{TL} \Delta \ell}; \; V_x = V_2^i + V_4^i; \quad V_z = V_1^i + V_3^i \quad (1.84)$$

where $\hat{Z} = 4 + Z_S$ *and* $Z_S = 4(\mu_r - 1)$. The characteristic impedance of each individual transmission line, Z_{TL} becomes $Z_o / \sqrt{2}$, where Z_0 is the characteristic impedance of the free space. The propagation medium has the relative permeability of 1 but the relative permittivity of ε_r. So, by duality, the normalized impedance of the short-circuited stub, Z_s becomes $Z_S = 4(\varepsilon_r - 1)$, meaning that the short circuited stub models the permittivity of the medium.

The implementation of TD simulations is as follows:

- A source with a chosen spatial altitude distribution, having a pulse character in time (that yields broad band analysis with a single simulation), is injected via the necessary field components.
- Earth's surface effects are included either as a terrain profile or a smooth impedance boundary.
- In order to implement a non-homogeneous atmosphere, a refractivity profile over the earth's surface (including earth's curvature) is introduced via relative permittivity of the air, $\varepsilon_r=n^2(x,z)$.
- One-way propagation is traced via a 2D rectangular sliding window. The content of this propagation window is the pulse that carries information related to terrain scattering, refractivity effects, and surface losses.
- The sliding propagation window moves from left to right in the computation space and circulates back to the left when reaches the right most-end, which is the initial profile of the next computation space.
- The process and TD simulations repeat until the wave longitudinally propagates to a desired range. The algorithm stores necessary information (such as range, terrain profile, transverse and/or longitudinal propagation characteristics at chosen observation points).
- Frequency-domain characteristics may be obtained from the TD simulations by off-line discrete Fourier transformation (DFT) analysis.

It should be noted that preparation of TDWP algorithm, based on FDTD plus PML termination, is quite straightforward. On the other hand, one needs to introduce modifications in TLM-WP algorithm [20]. First of all, 2D TLM computation space is constructed via a series node representation (see Fig. 1.14) to represent a TM_z problem. Although four-arm node is shown in the figure, the fifth arm (with a short-circuit termination) is also used to model permeability of the node, which in turn represents permittivity because of the duality principle. Secondly, the FDTD-PML algorithm, prepared for TDWP, is used in TLM-WP to absorb scattered fields [20,41]. In order to do that, a transition cell is located between TLM computation space and FDTD-PML blocks, and field components of TDWP are matched to the voltage pulses of TLM-WP in this cell, unlike [41], where overlap cell is directly taken as the first cell in FDTD-PML region. Also, attention should be paid in matching FDTD fields to TLM voltage pulses at the left FDTD-PML-TLM interface, since FDTD field components in a cell are not symmetrically located as the voltages are in the TLM node. If for example, $k = m$ (in the z-direction) is the overlap cell, then vertical electric field component (E_x) of the next cell ($k = m+1$) should also be used to write down TLM voltages in terms of FDTD fields (or vice versa).

The implementations of non-flat PEC terrain and surface impedance in TD propagators are as shown in Fig. 1.15. Here, the FDTD implementation is given. The staircase approximation is used to model non-flat longitudinal terrain profile in both simulators. It is achieved by forcing all tangential electric field components (E_x at vertical edges, E_z at horizontal edges for boundary cells and both for the inner cells) to be zero during the TDWP simulation. In TLM-WP, it is performed by using the short-circuit (SC) scattering matrix in the irregular terrain regions [20].

Although PEC boundary approximation is mostly adequate at VHF and above (i.e., frequencies higher than 100 - 150 MHz), accurate impedance boundary simulations are essential at HF frequencies and below. A propagator should be capable of handling imperfect surface effects including multi-mixed path propagation (e.g., land - sea transition). This is achieved by surface impedance modeling as explained in [42]. The first magnetic field component above the impedance boundary (i.e., the magnetic field component at first 2D-FDTD cell over the surface) is calculated from its value at previous time-step plus two neighboring vertical and one horizontal electric fields by using surface impedance relation in terms of the resistance R_s and reactance L_s components [42].

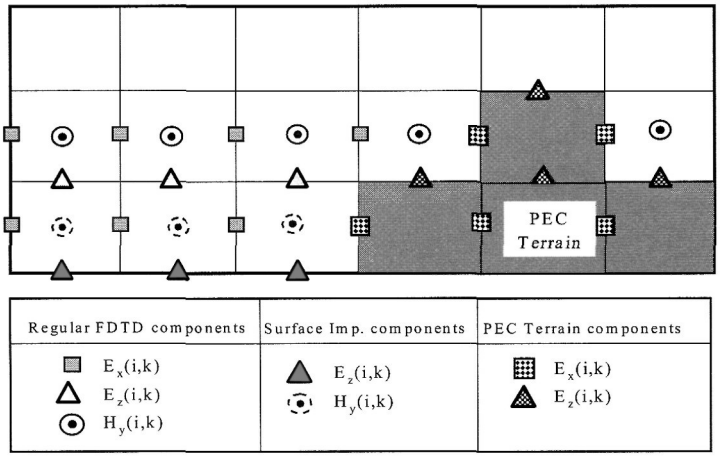

Figure 1.15: *Non-flat terrain and surface impedance modeling*

In TDWP implementations, the first magnetic field component above the impedance boundary is calculated from

$$H_y^{n+1/2}(i,k) = \frac{1 - R_s \Delta t / 2\mu_0 \Delta x - L_s / \mu_0 \Delta x}{1 + R_s \Delta t / 2\mu_0 \Delta x - L_s / \mu_0 \Delta x} H_y^{n-1/2}(i,k)$$
$$- \frac{\Delta t}{\mu_0 \Delta z (1 + R_s \Delta t / 2\mu_0 \Delta x - L_s / \mu_0 \Delta x)} \left[E_x^n(i,k+1) - E_x^n(i,k) \right] \quad (1.85)$$
$$+ \frac{\Delta t}{\mu_0 \Delta x (1 + R_s \Delta t / 2\mu_0 \Delta x - L_s / \mu_0 \Delta x)} \left[E_z^n(i+1,k) \right]$$

instead of (1.82), while E_z on the surface is set to zero. For a highly conducting medium (i.e., $\sigma >> \omega\varepsilon$) surface parameters may be approximated as

$$R_s = \sqrt{\frac{\omega\mu}{2\sigma}}, \qquad L_s = \sqrt{\frac{\mu}{2\omega\sigma}}, \quad (1.86)$$

but

$$R_s = \frac{\sqrt{\mu}}{\sqrt[4]{\varepsilon^2 + \frac{\sigma^2}{\omega^2}}} \cos\left[\frac{1}{2}\arctan\left(\frac{\sigma}{\omega\varepsilon}\right)\right] \tag{1.87a}$$

$$L_s = \frac{1}{\omega}\frac{\sqrt{\mu}}{\sqrt[4]{\varepsilon^2 + \frac{\sigma^2}{\omega^2}}} \sin\left[\frac{1}{2}\arctan\left(\frac{\sigma}{\omega\varepsilon}\right)\right] \tag{1.87b}$$

should be used if the medium is not highly conducting and $\sigma \approx \omega\varepsilon$.

It should be noted that the tangential electric and magnetic field components are related via a frequency-dependent surface impedance given in terms of frequency-dependent R_s and L_s values, as follows:

$$E_z(\omega) = Z_s(\omega) H_y(\omega) \tag{1.88}$$

$$Z_s(\omega) = R_s(\omega) + jX_s(\omega), \quad X_s(\omega) = \omega L_s(\omega) \tag{1.89}$$

where $\omega = 2\pi f$ and f denotes the frequency. On the other hand, their TD values are required in TDWP simulations. This makes a convolution process necessary in TD, which means extra computation time; therefore an approximation is implemented to eliminate the convolution process. Numerical values of R_s and L_s are calculated from the definition of surface impedance in terms of lossy ground parameters ε and σ, at the center frequency of the band of the source pulse and are assumed to be constant [42]. As mentioned before, the same surface impedance routine is also used in TLM-WP by means of using a connection (transition) cell [24] between TLM computation space and surface boundary (It should be noted that non-flat PEC terrain and surface impedance effects are modeled separately in this study. Implementation of a non-flat imperfect terrain is quite straightforward, yet not implemented.)

1.4 APPLICATIONS WITH CANONICAL TEST CASES

All the methods presented here are tested with characteristic scenarios and comparisons are done among them within range of their validity. Ducting, antiducting, elevated ducting, etc., atmospheric conditions are used together with different non-flat terrain profiles.

In the simulators TDWP and SSPE, both earth's curvature and standard atmosphere condition can be included by using $n(x) = n_0 + x/a_e$, where $a_e = 4a/3 = 8504$ km is the effective earth's radius. Refractive index is either defined as $n = n_0(x) + x/a$ (where $n_0(x)$ is the refractive index height profile for flat earth), in order to take into account the effects of earth's curvature for all variations of atmospheric refractivity index, or an equivalent fictitious medium is introduced, where N as defined in (1.1) is replaced by the modified refractivity M as given in (1.3), where height is given in km. For the standard atmosphere (i.e., for a vertical linearly decreasing refractive index), N decreases by about 40 N unit/km while M increases by about 117 N unit/km. Sub-

refraction (super-refraction) occurs when the absolute value of the rate of change is less (more) than 40 N unit/km (79 N unit/km) for the refractivity, *N*. When the *N* lapse rate is less than -157 N unit/km ducting occurs. Sub, super, and standard atmosphere, and ducting conditions are pictured in Fig. 1.16.

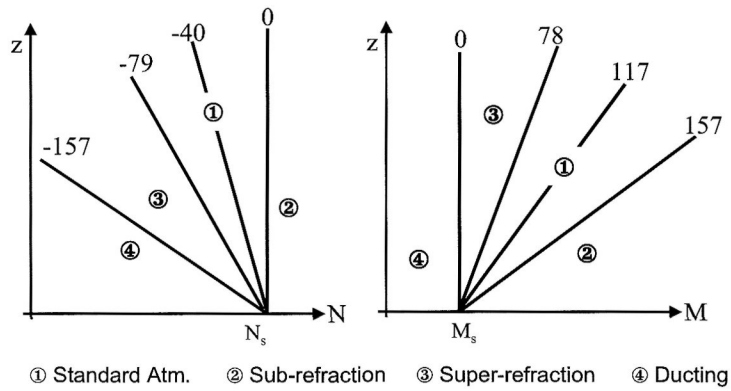

Figure 1.16: *Vertical refractivity variations and sub, super, standard atmosphere and ducting condition definitions*

All the comparisons given in this section are presented either propagation factor or path loss vs. height or vs. range. Propagation factor is defined as the ratio of electric fields computed under realistic surface and atmospheric conditions and fields computed in free space (E/E_0). This is straightforward in analytical computations. In TDWP, propagation factor is simulated as pictured in Fig. 1.17. First, the simulation is run for propagation over ground including refractivity conditions, and $E(t)$ vs. range (at constant height) or height (at a given range) is stored For this run, top, left and right of the computation space are terminated with PML blocks (see the top figure).

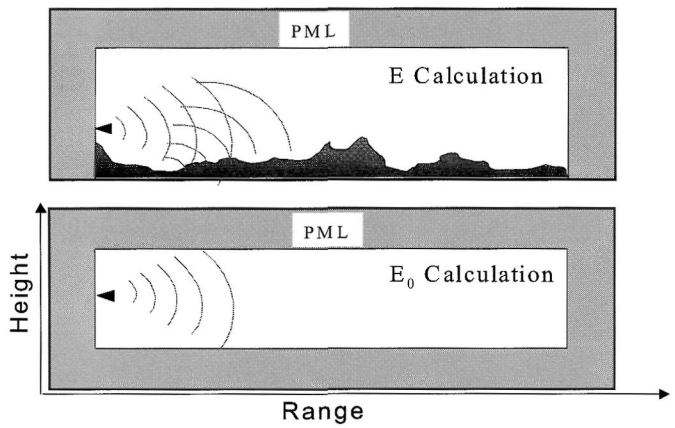

Figure 1.17: *Scenario for numerical propagation factor simulations in TDWP*

Then, the bottom boundary is removed and simulation is repeated assuming free-space propagation ((see the bottom figure).). In this case, $E_0(t)$ vs. range (at constant height) or height (at a given range) is stored. In the second run, the whole computation

space is terminated by PML blocks. Moreover, source and observer locations are shifted up until mid heights, so that unwanted reflections from the bottom PML block does not affect the results. Finally, they are Fourier transformed and frequency variations are obtained. This procedure is tested to remove a good amount of noise components, since errors introduced by imperfect PML blocks cancel each other.

In SSPE, a similar procedure is applied to calculate propagation factor. First, SSPE is run over ground including refractivity and E is obtained at the desired frequency for the required boundary condition, which is satisfied by extending the initial vertical profile odd (i.e., Dirichlet) or even (i.e., Neumann) symmetric with respect to $x = 0$ axis (see Fig. 1.18a). Then, E_0 is calculated for free space by forcing the initial vertical profile to be zero for $x < 0$ (see Fig. 1.18b).

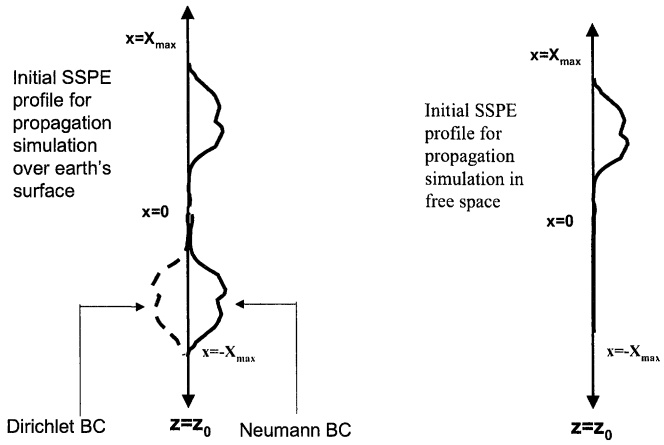

Figure 1.18: *Initial vertical profiles for (a) propagation over the earth's surface and (b) propagation in free space*

Path loss $L_p(z)$ is defined at $z = d$ as

$$L_p(d) = 10\log_{10}\left(\frac{P_t}{P_r(d)}\right) \quad [\text{dB}], \tag{1.90}$$

where P_t and P_r are the transmitted (at $z = 0$) and received (at $z = d$) powers, respectively. For excitation by a short electric dipole with a moment of $M = 5\lambda/2\pi$, corresponding to $P_t = 1$ kW, the received power for an isotropic receiver at $z = d$ can be determined from the computed field strength E for an isotropic receiver via

$$P_r(d) = \frac{E_r(d)^2}{Z_0} \times \frac{\lambda^2}{4\pi} \tag{1.91}$$

This leads to the expression

$$L_p(d) = 142.0 + 20\log_{10}(f_{MHz}) - 20\log_{10}(E_{\mu V/m}) \quad [\text{dB}] \tag{1.92}$$

with the frequency and field strength measured in MHz and dBμV/m, respectively. Frequency-domain characteristics can be obtained from the TD simulations. The algorithms store necessary information (such as range, terrain profile, transverse and/or longitudinal propagation characteristics at chosen observation points) while propagating from left to right. For example, a vertical field distribution (or propagation factor) at a given range can be obtained as follows:

- During the TDWP and/or TLM-WP simulation, time domain propagation data such as $E_x(x_i,t_j)$ at discrete x_i (i = 1,2, ...) observation heights and discrete t_j (j = 1,2, ...) simulation instants is accumulated at a desired range.

- The accumulation continues until all transients fade away.

- After TDWP simulation, height field distribution $E_x(x_i,f_A)$ at a given frequency f_A is directly obtained by off-line DFT analysis.

1.4.1 Propagation Under Ducting Conditions

The TD propagators are first tested over smooth, spherical earth. The propagation region is characterized by longitudinally homogeneous, bi-linear vertical refractive index, n, with the gradient of $|dn/dx| = 10^{-3}$ [n unit/m] (i.e., decreasing between ground and 25 m and increasing over 25 m). The vertical distribution of the source is Gaussian with spatial extent ≈15 m and maximum at 26 m height (i.e., the vertical profile is non-zero between 18.5 m and 33.5 m). The temporal distribution is a once-differentiated Gaussian pulse with 200-MHz bandwidth centered at 200 MHz. A 1000 × 500 FDTD/TLM computation (corresponding to 100 m × 50 m physical) space is used. A 1000 × 250 virtual window circulates 20 times as if the longitudinal number of cells in FDTD/TLM computation space is 5000. Instant snapshots are taken at different simulation times and are plotted as field profiles at different ranges in Fig. 1.19 (each plot is normalized to its maximum value).

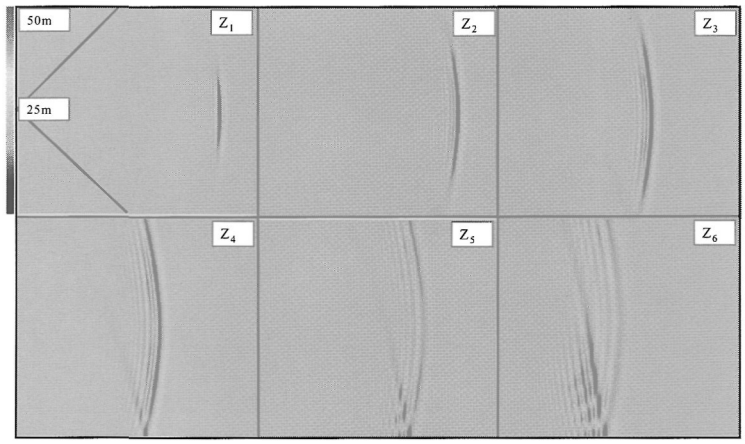

Figure 1.19: *TD pulse propagation inside the sliding window at propagation ranges Z_1, Z_2, ..., Z_6. Z_1: 670th time step ≈ 50-m range; Z_2: 1570th time step ≈ 110-m range; Z_3: 2250th time step ≈ 155-m range; Z_4: 2580th time step ≈ 180-m range; Z_5: 3070th time step ≈ 215-m range; Z_6: 4330th time step ≈ 305-m range*

The relevant wave constituents are the direct, ground-reflected and surface waves whose wavefronts and their interference (wave maxima and minima) appear as 2D images. As shown in the figure, the wave propagates to the right and is above the ground (at $z = Z_1$). While it is propagating it spatially extends because of cylindrical spreading and reaches the bottom surface (at $z = Z_2$ and $z = Z_3$). Then it reflects from the surface, giving rise to interference between the leading direct and trailing ground-reflected waves (as observed at $z = Z_4$ through $z = Z_6$).

Time histories of the pulse during propagation are accumulated at different ranges and along two constant heights; they are plotted in Fig. 1.20, where the results of both TDWP and TLM-WP are almost indistinguishable. In Fig.s 1.20a and 1.20b, the receiver heights are chosen to be 13 m and 35 m above the ground, respectively. Three plots correspond to the 94 ns time histories (i.e., signal vs. time) at three different ranges. Since the scale in each plot is normalized to its maximum value in order to reveal the detailed pulse shapes along the entire trajectory, relative field strengths with respect to the first window are also included as dB values in the plots. At $z = 23.5$ m, only the initial pulses appear inside the 94 ns propagation windows because the delay of the signal caused by the path difference (distance between direct and ground reflected pulses) exceeds the window length. As the distance increases, the path difference decreases and the ground-reflected pulse also appears inside the 94 ns propagation windows, as shown in the second windows. Inside the last windows the direct and ground-reflected pulses are almost indistinguishable.

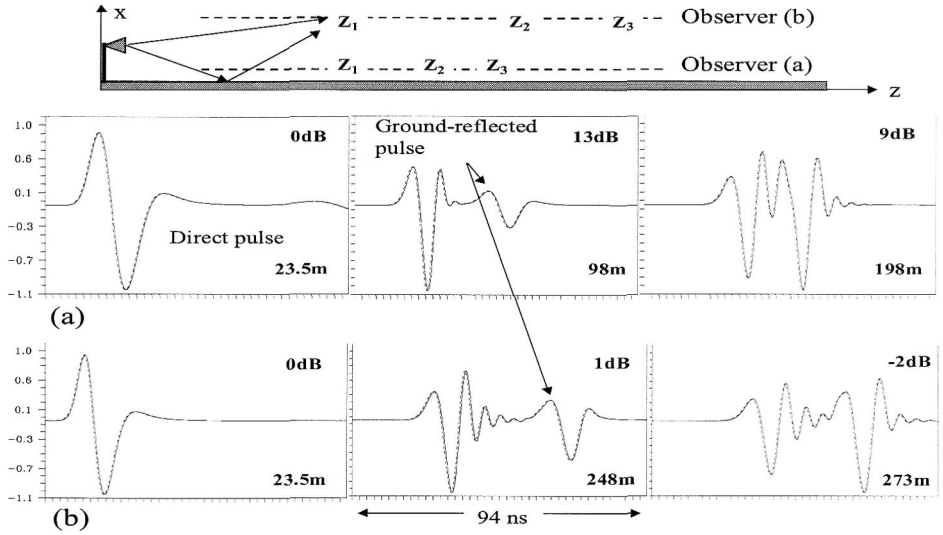

Figure 1.20: *Time histories of the pulse in Fig. 1.19 observed at different ranges along (a) 13 m, (b) 35 m above the surface. Solid: TLM-WP; dashed: TDWP*

TD results are transformed to Fourier domain (FD), and propagation factor vs. height variations are plotted in Fig. 1.21, where TDWP, TLMWP and SSPE are compared. Here, a fictitious tri-linear vertical refractivity is chosen with refractive index gradients between ground and 15 m, 15 m - 25 m and above 25 m as dn/dx=-1.2×10^{-5}, 5×10^{-6} and -1.2×10^{-5}, respectively. The spatial distribution of the source is Gaussian at a

height of 15 m, with spatial extent of ≈12 m. Temporal distribution is a once-differentiated Gaussian pulse in TLM-WP and TDWP. This short pulse has 200-MHz bandwidth centered at 200 MHz. The SSPE propagator, with the same spatial source distribution, is run separately for each frequency. With these parameters, energy is mostly trapped along the surface and the pulse reaches to PML blocks at larger distances compared to standard atmosphere. Therefore, numerical dispersion effect is dominant in this example.

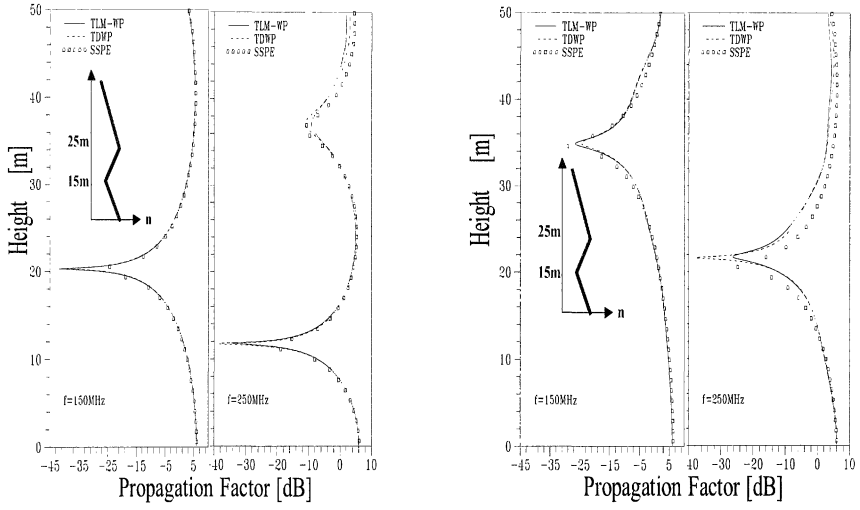

Figure 1.21: *$|E/E_0|$ vs. height after 25 and 45 sliding windows*

The first two plots belong to the results at a range of 625 m (311λ at 150 MHz and 518λ at 250 MHz). At these ranges the propagating pulse is still confined in the sliding window and the agreement is very good. On the other hand, the last two figures belong to a range of 1121.5 m reached at 45th window (561λ at 150 MHz and 935λ at 250 MHz), where the sliding window is hardly capable of holding the propagating pulse. Although the sliding window hardly bounds all the forward-propagated energy, very good agreement may still be obtained in frequency domain as long as most of the dominant contribution is traced.

1.4.2 Propagation Over Non-Flat Terrain

The TDWP is then compared against SSPE in propagation scenario that includes non-flat terrain. A scenario with strong forward scatter (and negligible backward propagation) is chosen in order to make comparisons with SSPE possible. A downward sloping terrain (200 m high at the source point and 0m at 5.5 km) plus smooth surface over which exists a vertical tri-linear, longitudinally homogeneous refractivity profile is taken into account.

A 1500 × 1000 TDWP computation space corresponding to 2250 m height and 1500 m range (with 1.5 m spatial discretization) is chosen. The initial field distribution is a once-differentiated Gaussian function with 15 MHz bandwidth at 10 MHz center frequency. A tri-linear vertical refractive index with n_0=1.0003 at the surface, dM/dx = 120 M/km up to 250 m, dM/dx = -50 M/km between 250 m and 400 m and dM/dx =

118 M/km above 400 m (with respect to the bottom of FDTD computation space) is chosen. Here, dM/dx is the gradient of atmospheric refractivity modulus. The spatial distribution of the source is Gaussian at an altitude of 300 m over the terrain. A 1500 × 500 virtual window circulates 13 times and extends the longitudinal number of cells in FDTD computation space to 6500. In Fig. 1.22, instant snapshots of field profiles taken at different simulation times are plotted at ranges Z_1 to Z_6, respectively. Pulse propagation (Z_1), surface reflection (Z_2), energy split (Z_3 and Z_4), and surface and elevated duct formation (Z_5 and Z_6) are clearly observed in Fig. 1.22.

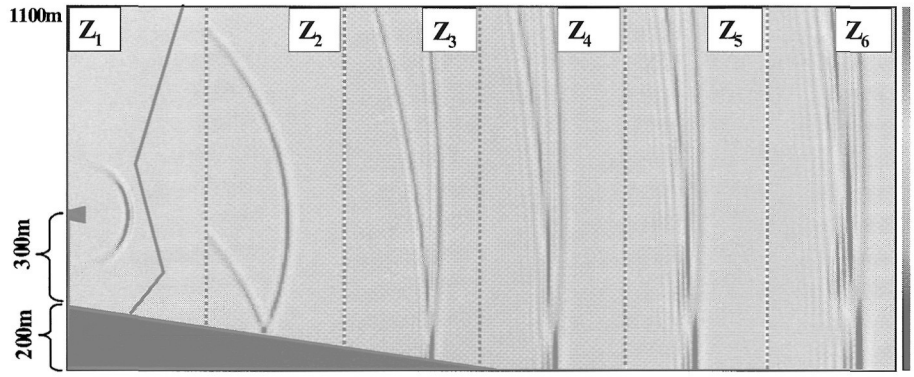

***Figure 1.22:**. Signal strength vs. range-height over terrain in TD (TDWP)*

Same source pattern is fed into the SSPE algorithm and is propagated through the same medium. In Fig. 1.23, the range-altitude field distributions at 10 MHz are plotted.

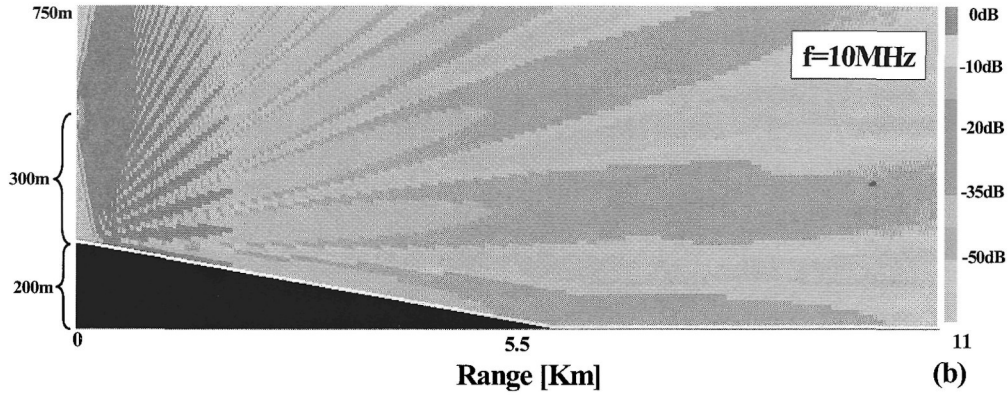

***Figure 1.23:**. Signal strength vs. range-height over terrain in TD (SSPE)*

Propagation factor vs. height for the same environment as in Figs. 1.22 and 1.23 are plotted in Fig. 1.24. Neumann boundary condition is applied for SSPE to model VED excitation as in TDWP. A good agreement between TDWP and SSPE is clearly observed. Propagation factor vs. height over a PEC level terrain with the same tri-linear refractivity profile, computed via SSPE, is also given in the figure (dashed curves) to emphasize the effects of the downward sloping terrain portion.

In Fig. 1.25 propagation factor vs. range computed with these three simulators are plotted in Fig. 1.25 for a more realistic scenario. Here, a 1.5-km-long non-flat terrain, with maximum height of 40 m is taken into account (see Fig. 1.25a). The source and observation points are 5 m above the ground and the mesh sizes are taken as 10 cm.

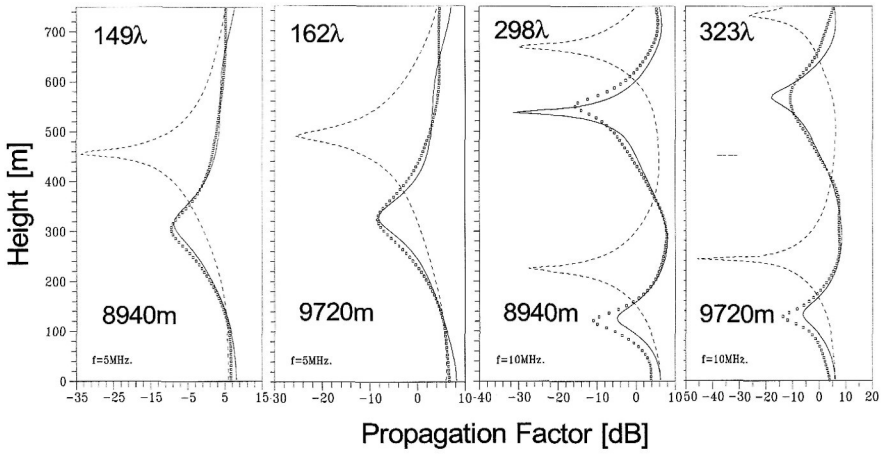

Figure 1.24:. *$|E/E_0|$ vs. height at 10 MHz and 15 MHz and at two observation ranges (solid: SSPE; dots: TDWP, dashes: SSPE over level surface).*

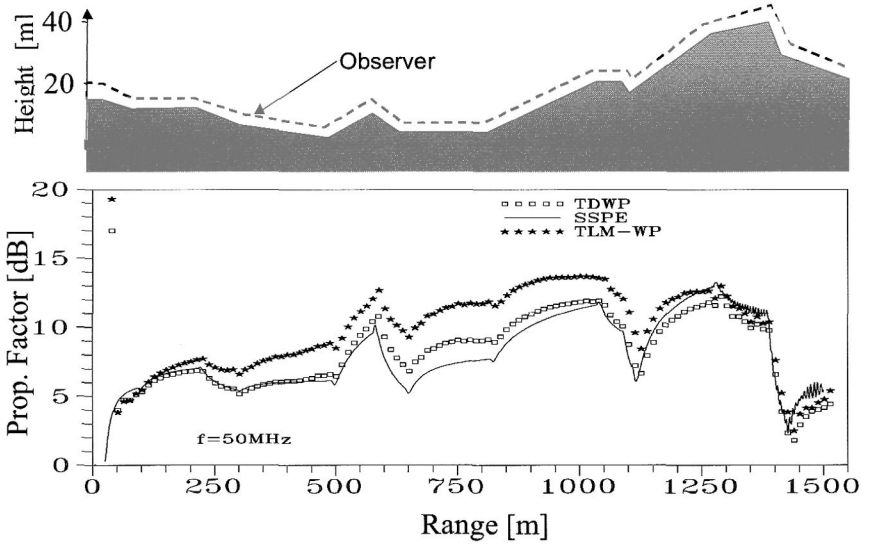

Figure 1.25: *$|E/E_0|$ vs. range for the typical non-flat terrain*

Although SSPE does not include the back-scatter effects, TDWP and TLM-WP results contain local back-scatter contribution as long as it is within the sliding window. This explains the discrepancy between SSPE and TD propagators. As seen in Fig. 1.25,

there is also a discrepancy between the magnitudes of TDWP and TLM-WP, which is not observed for propagation over smooth ground. This can be because of numerical dispersion or differences in abilities of the FDTD and TLM implementations themselves, resulting in different responses to the scattering mechanisms, such as reflection, edge/tip diffraction, multi-path interference, and surface waves, which is under investigation.

1.4.3 Urban Wireless Communication

TD propagators are also applicable in wireless communications when the depths of the buildings are assumed large enough to reduce the problem to a 2D case. The power of the TD propagators arises from their applicability in wireless communication in urban regions, such as along a narrow street with tall buildings in different sizes. In this section this is presented on various scenarios.

In most of the practical problems, maximum ranges of interest in urban areas cannot be covered by one or a few sliding windows. Therefore, while the sliding window is tracing the longitudinally propagating component, backward and upward propagated waves are also traced as long as they are confined inside the sliding window. There may still be backward and upward scattered contributions at observation points where the window has already passed. Because of this inefficiency, time domain propagators are called to handle local back and up scattered components. In order to show these effects, a scenario in Fig. 1.26 is taken into account.

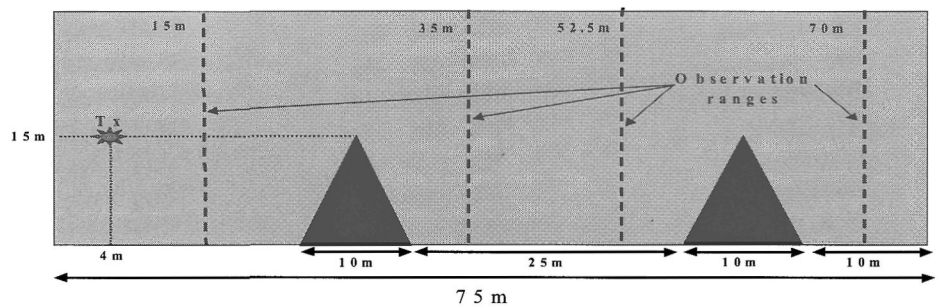

Figure 1.26: *A scenario with two wedge-shaped PEC obstacles (base = 10 m, height = 15 m). Transmitter is located 15 m above the PEC ground*

Here, two 15-m-tall PEC triangular buildings having 10 m base lengths are separated with a distance of 25 m. The other dimensions and source and observation locations are denoted in the figure. The mesh size is 1 cm. The same Gaussian source is used and TD propagation along the buildings is simulated in two ways: (i) with a unique FDTD space (without sliding), (ii) with two sliding windows via TDWP and TLM-WP. The results are given in Fig. 1.27, as propagation factor vs. height at four observation ranges (it should be noted that these results belong to a single time-domain simulation plus multiple DFT application). In the figure, observation ranges from left to right are numbered from 1 (at 15 m) to 4 (at 70 m). Almost indistinguishable solid and dashed lines correspond to TDWP and TLM-WP computations, respectively, while the dashed line represents single window FDTD computations. It is clearly observed in the figure that, although TDWP and TLM-WP results have indistinguishable agreement, they do not agree very well with the FDTD, which may be assumed as a reference solution.

Moreover, unacceptable discrepancies appear at some heights and ranges. Here, FDTD results represent reference solutions (since the numerical dispersion ratio is 60 at 50 MHz), and the reason of the discrepancies may easily be understood from the scenario given in Fig. 1.26. The strongest back- and up-scattered components are expected to be at the first observation range, at the bottom and at heights above the source (because of the inclined wall of the wedge type building). Not so strong as the dominant scatter, back- and up-scattered components are also expected in between the buildings. On the other hand, at the last observation range the forward propagating wave is dominant, therefore, as expected, the best agreement is obtained at this range.

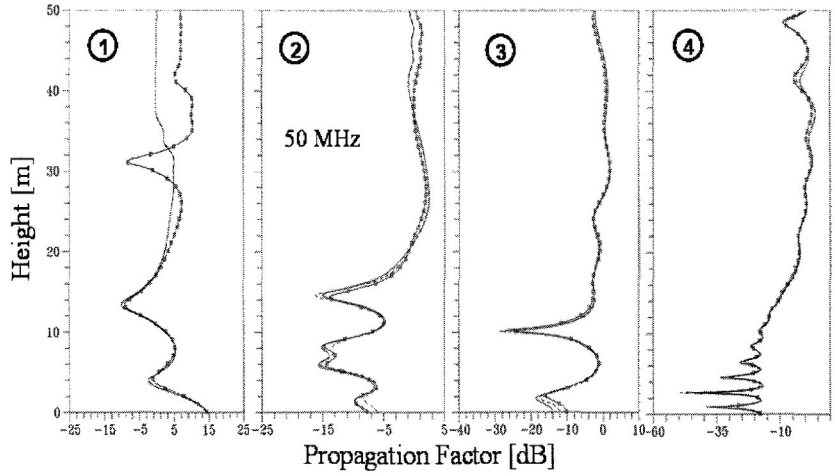

Figure 1.27: *|F| vs. height at 50 MHz at four observation ranges mentioned in Fig. 1.26. Solid, TDWP; Dashed, TLM-WP; Solid with dots, FDTD*

Longitudinal variations of field strength are also calculated via TDWP and TLM-WP and are presented in Fig. 1.28 at 15-m height and for 50 MHz.

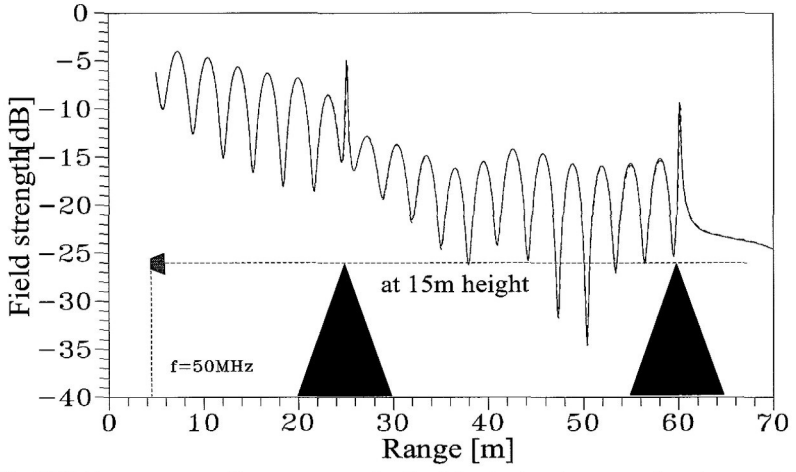

Figure 1.28: *$|E/E_0|$ vs. range for a scenario that includes two wedge-type obstacles*

As seen, although range variations are highly oscillatory almost perfect agreement is obtained between TDWP and TLM-WP results. It is also interesting to observe tip-diffracted components (two peaks at ranges 25 m and 60 m, which correspond to the tips of the buildings) in the 50 MHz figure. Finally, a complex scenario, where four different-shaped buildings with different sizes are used, is taken into account as given in Fig. 1.29.

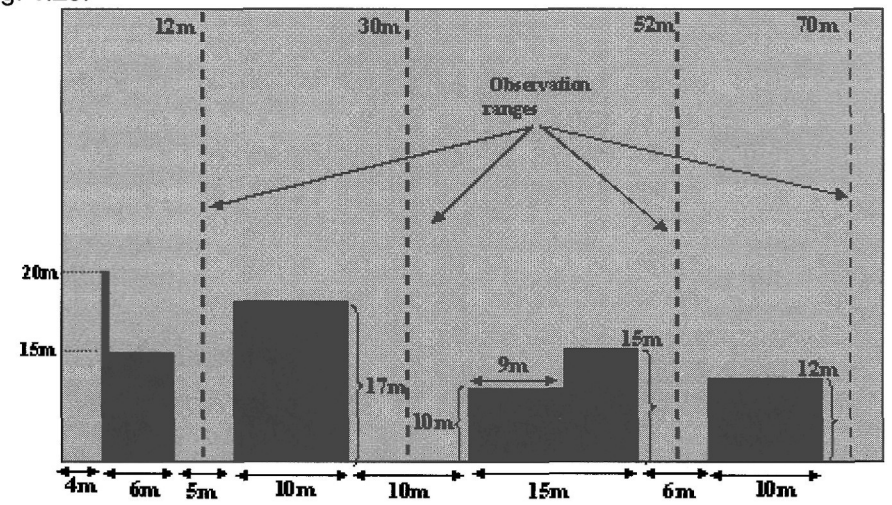

Figure 1.29: *A scenario with multiple buildings and four observation ranges. The transmitter is located at top of the first building (i.e., 20 m above ground)*

All dimensions and source/observation locations are mentioned in the figure. The buildings are assumed to be PEC. The results are presented in Fig. 1.30 as propagation factor vs. height at given four observation ranges. Both TDWP and TLM-WP computations are carried out within a unique FDTD/TLM computation space (to account for all scattered contributions).

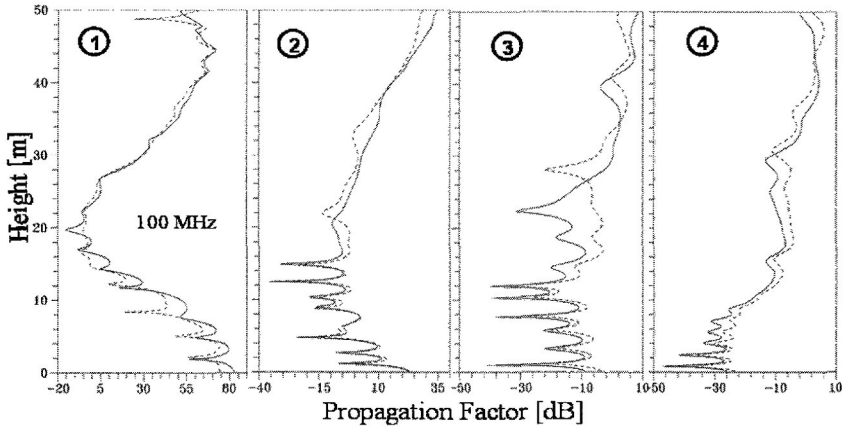

Figure 1.30: *$|E/E_0|$ vs. height at 100 MHz at four observation ranges mentioned in Fig. 1.29. Solid, TDWP; Dashed, TLM-WP*

The results do not agree very well as observed in the previous examples. There is no discretization error in this example, since all the buildings are chosen to be rectangular. Possible sources of these discrepancies are (i) numerical dispersion errors (it may require numerical dispersion ratios higher than 30 at 100 MHz), (ii) PML termination (since the scattering mechanisms, such as reflection, edge/tip diffraction, multi-path interference, surface waves, etc., become complex in this example), or (iii) differences in abilities of the FDTD and TLM implementations themselves.

The screen captures of TD pulse scattering at different time instants for the same scenario is given in Fig. 1.31 as signal strength vs. range/height. Since very similar results are obtained, only TDWP results are pictured in this figure. The multi-reflections, edge and tip diffraction and ringing in between buildings are clearly observed in the figure.

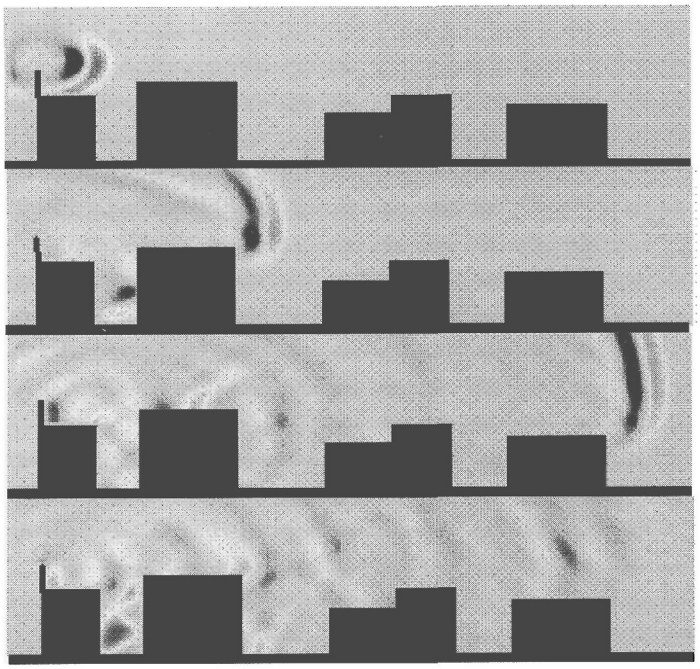

Figure 1.31: *A 3D picture of pulse scattering along the street*

1.4.4 Surface Waves and Mixed-Path Propagation

Although a perfectly reflecting boundary assumption provides in general sufficient approximation at VHF and above (i.e., frequencies higher than 100 - 200 MHz), the use of impedance boundary condition becomes essential at HF frequencies and below. This is especially required for the simulation of long-range marine communication and/or ocean surveillance systems using HF frequencies. A challenging problem is to predict surface wave path loss variations over mixed paths, such as sea - land or sea - land - sea (island) transitions. A sharp decrease occurs in signal strength along sea - land transition and the signal recovers itself after land - sea transition (beyond the island), known as the Millington (recovery) effect [5]. A propagator should be capable of handling these effects in mixed-path simulations.

Data generated via approximate analytical (ray-mode) solutions is used for the validation of the TDWP augmented with the implementation of the impedance boundary condition on the ground surface. Two typical scenarios and the results obtained with TDWP simulations are given in Figs. 1.32 and 1.33. In Fig. 1.32, a sea - land transition problem for a standard atmosphere including earth's curvature (i.e., *dM/dx* = 118 M/km) is taken into account and range versus surface wave path loss (when both transmitter and receiver are at the surface) are plotted at 15 MHz.

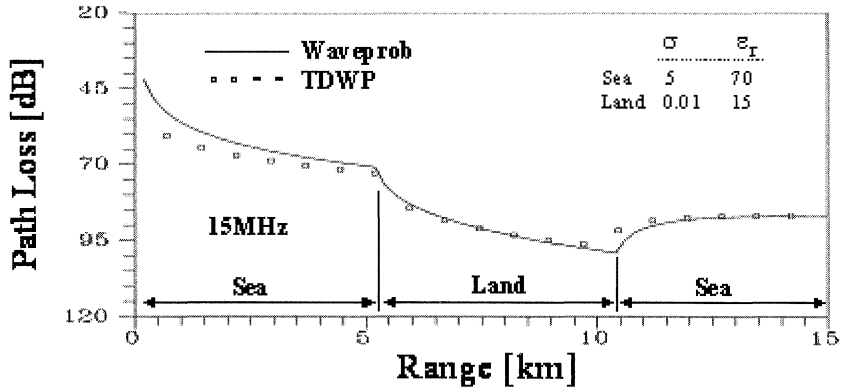

Figure 1.32: *SW path loss vs. range over mixed-path (sea - land transition, the first 8.2 km is sea and the rest is land) at 15 MHz*

The first 8.2 km is assumed to be sea and the rest is land (the parameters of the land and sea are taken as σ_g = 0.01 [S/m], ε_g = 15 and σ_g = 5 [S/m], ε_g = 70, respectively). Ray - mode results are also shown in this figure and serve as reference solutions. A vertical short electrical dipole (with a dipole moment of $5\lambda/2\pi$ Am, corresponding to a 1 kW transmitter) is used in analytical solution and TDWP results are normalized to this value. A very good agreement between the results is clearly seen in the figures. It should be noted that TDWP results at both frequencies belong to a single pulse propagation simulation followed by two off-line DFT applications.

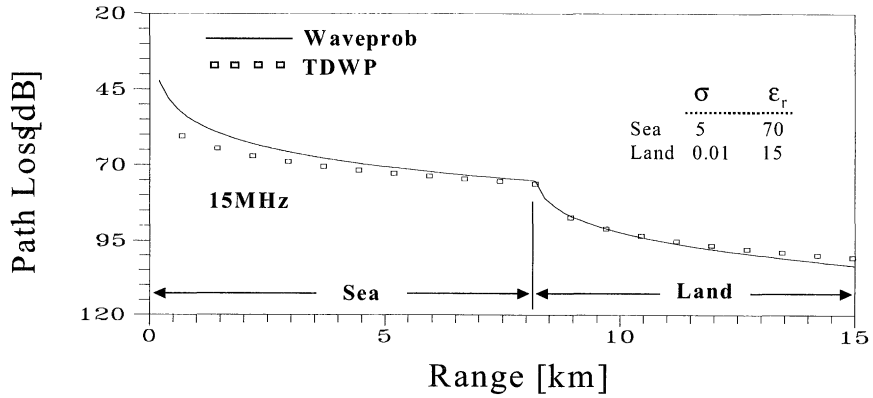

Figure 1.33: *SW path loss versus range over mixed-path (island transition, a 5.2 km length island 5.2 km away from the source) at 15 MHz*

In Fig. 1.33, the results of a scenario corresponding to ground wave propagation over a path including an island transition under the assumption of standard atmospheric conditions are plotted. A 5.2-km length island is assumed to be 5.2 km away from the transmitter. Again, range versus surface wave path loss are plotted at 15 MHz with the same land and sea parameters. Also in this case the results agree very well.

1.5 NUMERICAL SIMULATORS

Five simulator packages are prepared for the reader who wants to exercise different ground wave propagation scenarios. Three of them (GRWAVE, HFMIX, and KNIFE) are based on ray-mode approach and the other two are SSPE in FD and TDWP in TD.

Ray-mode formulations in (1.44) - (1.46) and (1.58) can be combined in an intelligent way to extend ranges of their individual validity and uniformizes the solution in *interference, intermediate and diffraction regions* [WAVEPROB]. Here, *simple sample* simulators are presented which can be used in these regions, separately. GRWAVE is valid over lossy spherical earth's surface, only in interference region, where transmitter and receiver is within LOS. HFMIX is prepared for surface-wave path loss calculations which can handle multimixed-paths beyond the diffraction region. Transmitter and receiver height effects are augmented into HFMIX as height gain functions (as given in (1.58)). KNIFE uses four rays to account for single knife-edge diffraction effects as described in [43]. Surface impedance and roughness are also taken into account in KNIFE.

1.5.1 GRWAVE: LOS Ray Code

The flow chart of GRWAVE is given in Fig. 1.34. The simulator reads user-supplied input parameters from the input file GRW.INP, runs and outputs the results in two different output files: GR-R.DAT as range vs. propagation factor [dB] and GR-H.DAT as height vs. propagation factor [dB].

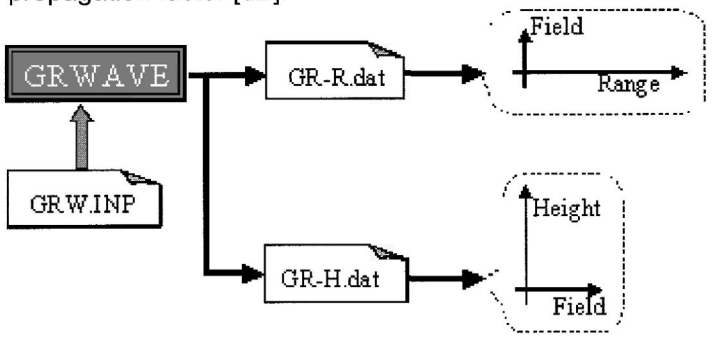

Figure 1.34: *The structure of GRWAVE*

The GRW.INP input file contains five rows of parameters, which are listed in Table 1.2. The fifth line has four real numbers A, B, C, and D, which correspond to range [km], first height [m], last height [m] and height increment [m] when scenario type is 1, and to height [m], first range [km], last range [km] and range increment [km] when scenario type is 2, respectively.

Two typical examples obtained via GRWAVE are pictured in Figs. 1.35 and 1.36. In Fig. 1.35, propagation factor vs. range is plotted and the input parameters are as follows:

GRW.INP (Fig. 1.35)	LINE 1:	500
	LINE 2:	15, .01
	LINE 3:	500
	LINE 4:	2
	LINE 5:	100, 20.0, 120.0, 0.5

Table 1.2: The GRW.INP file and required parameters

Row No.	Parameter
1	Frequency [MHz]
2	Relative permittivity, conductivity
3	Transmitter height [m]
4	Scenario type (1, Field vs. height: 2, field vs. range)
5	A, B, C, D

Similarly, in Fig. 1.36, propagation factor vs. height is plotted. Here, GRWAVE is run three times at three different ranges. Input parameters are as follows:

GRW.INP (Fig. 1.36)	LINE 1:	500
	LINE 2:	15, .01
	LINE 3:	500
	LINE 4:	2
	LINE 5:	A, 0.0, 400, 0.5 (A=40, 80 and 120)

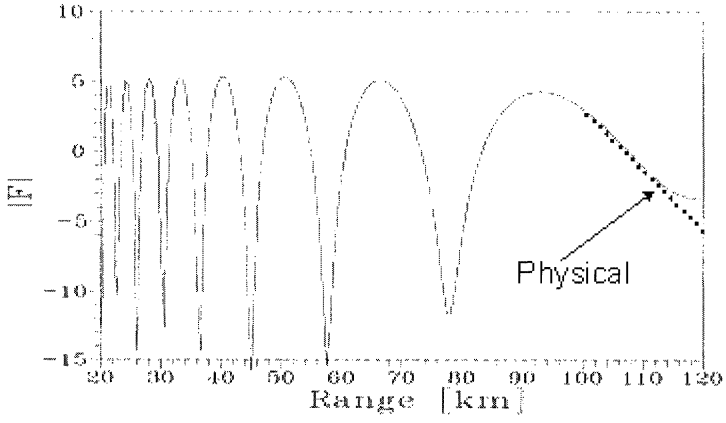

Figure 1.35: *$|E/E_0|$ vs. range at 100 m obtained with GRWAVE*

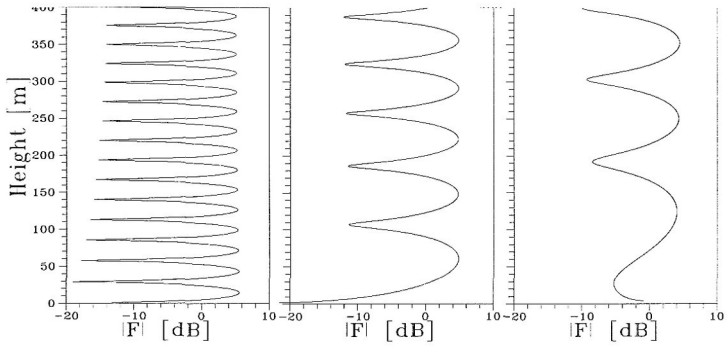

Figure 1.36 : *$|E/E_0|$ vs. height at 40, 80 and 120 km, respectively*

1.5.2 HFMIX: Surface-Wave Path Loss Predictor

The flow-chart of HFMIX is given in Fig. 1.37. The simulator reads user-supplied input parameters from the input file HFMIX.INP, runs and outputs the results in two different output files; LMIX.dat as range vs. path loss [dB] and EMIX.DAT as height vs. field values [dBμV/m].

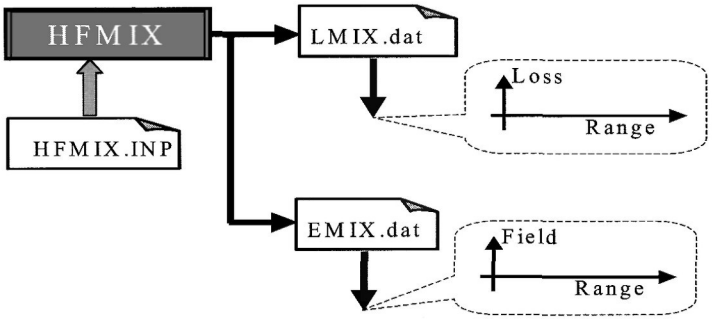

Figure 1.37: *The structure of HFMIX*

The HFMIX.INP input file contains a minimum of five rows of parameters, which are listed in Table 1.3. The user supplies a number of propagation sections in the fourth line in HFMIX.INP. Depending on this number path length, conductivity, and relative permittivity of each section is given in the fifth, sixth, seventh, etc., lines.

Table 1.3: The HFMIX.INP file and required parameters

Row No:	Parameter
1	Frequency [MHz]
2	Range increment [km]
3	Transmitter and receiver heights [m]
4	Number of propagation paths [Integer]
5	Path length, conductivity, relative permittivity

The scenario of HFMIX is pictured in Fig. 1.38. Total propagation path is automatically calculated when section lengths are specified by the user (e.g., $R = d_1 + d_2 + d_3 + d_4$)

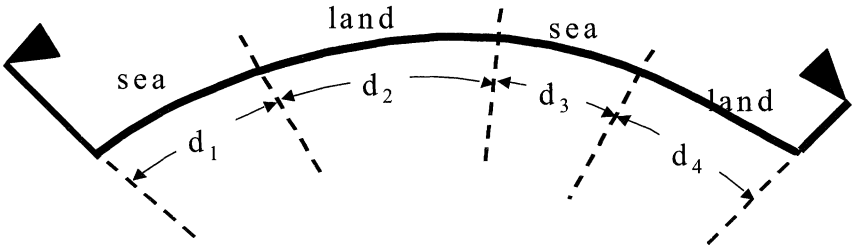

Figure 1.38: *HFMIX scenario definitions*

A typical HFMIX result is presented in Fig. 1.39, as path loss vs. range for a three-section propagation path (first 100 km sea, then an island of 50 km, and another 150 km of sea) at three different frequencies are plotted.

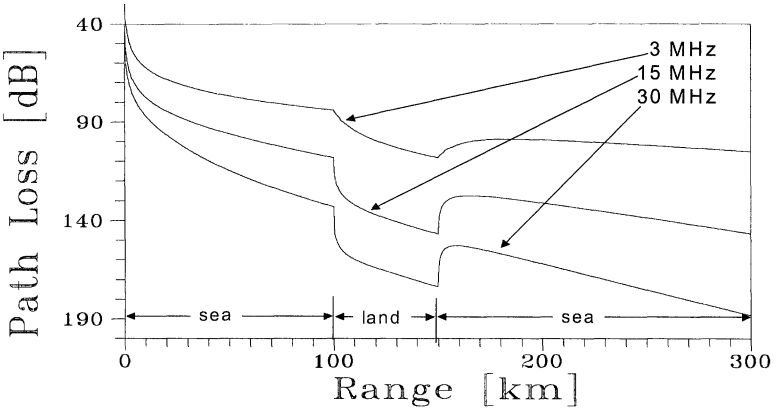

Figure 1.39: *Path loss vs. range over a three-section path*

Some remarks on HFMIX are listed as follows:

- Standard atmosphere over smooth spherical earth is assumed, therefore no refractivity variations are allowed.
- Only surface wave contribution is included. Transmitter and receiver heights are included as height gain functions.
- HFMIX can be best used from a few hundred kHz up to 40-50 MHz. In this frequency region, transmitter and receiver heights better be less than a hundred meters.
- Ground parameters are taken into account, but only two types of grounds are allowed. Mixed-path effects (Millington recovery) can be calculated for up to 10 different propagation sections.
- Homogeneous (single-section) ground, such as land or sea, can be given by giving "1" in the line 4 and total propagation length in the 5th line.

- Codes are calibrated against SSPE and CCIR [44] recommendations. There are no "shortcuts" while coding.
- Since this is an analytical-based code, no improvements are expected parallel to increase in computers' capabilities. Current PC's are fast enough to do computations.

1.5.3 KNIFE: Four-Ray Knife-Edge Code

Knife is a ray method prepared for a single PEC obstacle with zero thickness between a transmitter and a receiver. It uses four rays: the direct ray between the transmitter and receiver, the tip-diffracted ray from the top of the obstacle, te ground-reflected rays, and, finally, the ground-reflected ray behind the obstacle that reaches there via tip diffraction. KNIFE accounts for polarization and surface impedance, including a surface roughness factor. The details of this program can be found in [43].

The structure of this code is illustrated in Fig. 1.40. As usual, the package accepts user defined input parameters from the input file KNIFE.INP. The KNIFE.INP input file contains seven rows of parameters, which are listed in Table 1.4. A typical example is plotted in Fig. 1.41, for PEC surface at three different frequencies.

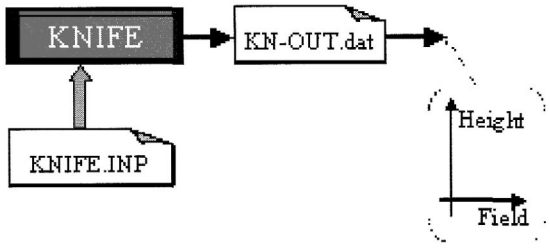

Figure 1.40: *The structure of KNIFE*

The KNIFE.INP file for this example is as follows:

KNIFE.INP (Fig. *1.41*)	LINE 1:	170, 600 and 1300
	LINE 2:	100
	LINE 3:	100, 10000, 5000
	LINE 4:	1, 250, 1
	LINE 5:	4.0, .0001, 4.0, .0001
	LINE 6:	0.0, 0.0
	LINE 7	1

Although relative permittivity and conductivity values are supplied in LINE 5, surface roughness for sections both on the left and right of the obstacle are set to zero in LINE 6. The polarization is horizontal for all these three plots.

Table 1.4: The KNIFE.INP file and required parameters

Row No:	Parameter
1	Frequency [MHz]
2	Transmitter height [m]
3	Obstacle height [m], TR to Obstacle distance [m], Obstacle to Rx distance [m]
4	First height [m], last height [m], height increment [m]
5	Relative permittivity, conductivity [Left part] Relative permittivity, conductivity [Right part]
6	Roughess factor (real number between 0-1)
7	1 [H polarization], 2 [V polarization]

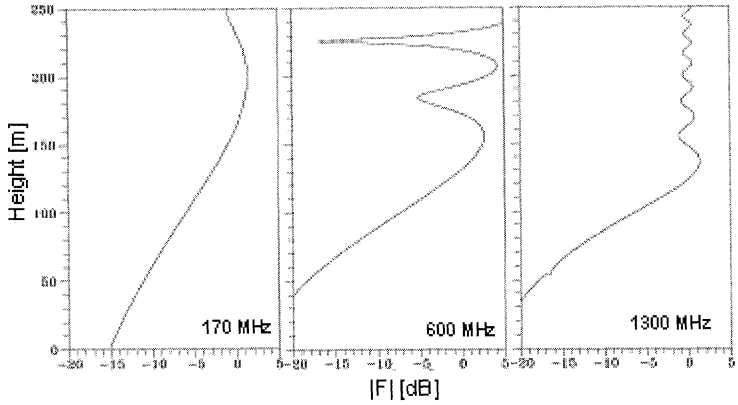

Figure 1.41: *$|E/E_0|$ vs. height at three different frequencies*

1.5.4 SSPE: Frequency- Domain Wave Propagator

SSPE package is capable of calculating propagation factor and path loss as a range and/or height profile. The structure is given in Fig. 1.42. Some remarks on the package are as follows:

- It uses Dirichlet-type boundary conditions at the surface, therefore source should be minimum 10 m above the surface.
- Dirichlet-type boundary condition for the scalar wave function correspond to TE_z type EM wave problem, therefore only horizontal polarization is possibly chosen.
- The package is better used for frequencies from 200 MHz up to 1 GHz. Maximum height is limited as 500 m, which is divided into 256 height steps.
- Because of the Nyquist criteria, the maximum frequency that can be used with this height step size is limited to approximately 1 GHz for accuracy up to propagation angle of $\theta = 4.5°$ with respect to horizontal axis *z*. For higher propagation angles, the operating frequency should be lower.

Again, the program requires that the user first supply the input file SSPE.INP. It runs and yields two output files RANGE.DAT (first column range [km], second column propagation factor [dB]), and HEIGHT.DAT (first column height [m], second column propagation factor [dB]). Optionally, CONTOUR.DAT may also be obtained, where 3D field data are used in a MATLAB file (PLOT3D.M) for plots as propagation factor vs. range/height is available. Necessary input parameters are listed in Table 1.5.

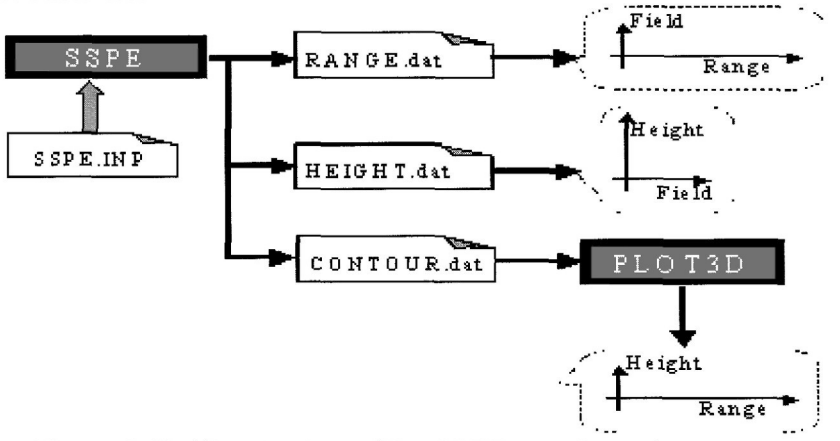

Figure 1.42: *The structure of the SSPE sample package*

Table 1.5: The SSPE.INP file and required parameters

Row No:	Parameter
1	Frequency [MHz]
2	Transmitter height [m]
3	Maximum range of interest [m]
4	Observation height [m]
5	Contour map (1: Yes, 0: No)
6	Scenario Type (1, single obstacle; 2, double obstacle)
7	**If Scenario Type is 1 (Single Obstacle)** Obstacle height [m], transmitter-to- obstacle distance [m], obstacle base length [m], obstacle type (1:wedge, 2: block)
7 – 8	**If Scenario Type is 2 (Double Obstacle)** Obstacle height [m], transmitter-to-obstacle distance [m], obstacle base length [m], obstacle type (1,wedge; 2, block) Obstacle height [m], distance between first and second obstacles [m], obstacle base length [m], obstacle type (1, wedge; 2, block)
8 (or 9)	Refractivity profile (1,2 or 3) 1: Standard atmosphere 2: Sub-refraction 3: Super-refraction

For example the SSPE.INP file given below belongs to Fig. 1.43. The parameters read are 400 MHz, source height h_v = 50 m, single obstacle, obstacle height h_{ter} = 100 m,

transmitter-to-obstacle distance d_1 = 5 km, obstacle base w_1 = 2000 m, maximum range of interest R_{max} = 10 km, observation height h_{obs} = 50 m, obstacle: wedge, vertical refractivity profile: standard atmosphere and no contour map data is required.

SSPE.INP (Fig. *1.43*)		
	LINE 1:	400
	LINE 2:	50
	LINE 3:	10000.
	LINE 4:	50
	LINE 5:	0
	LINE 3:	1
	LINE 4:	100,5000, 2000, 1
	LINE 5	1

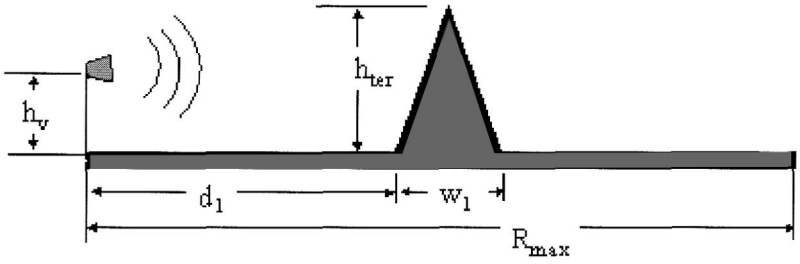

Figure 1.43: *The scenario of the SSPE.INP file in SSPE.INP given above*

Similarly, the scenario in Fig. 1.44 can be obtained with an input file given below (250 MHz, source height h_v = 10 m, double obstacle, wedge and block, wedge height h_{ter1} = 5 m, source-to-wedge distance d_1 = 500 m, wedge base w_1 = 5 m, block height h_{ter2} = 10 m, wedge-to-block distance = 50 m, block base w_2 = 5 m, maximum range of interest R_{max} = 1 km, observation height h_{obs} = 10 m vertical refractivity profile: standard atmosphere and contour map data are required).

SSPE.INP (Fig. *1.44*)		
	LINE 1:	250
	LINE 2:	10
	LINE 3:	1000
	LINE 4	10
	LINE 5:	1
	LINE 6:	2
	LINE 7:	5, 500, 5, 1
	LINE 8	10,50, 5, 2
	LINE 9	1

SSPE is applied to two typical propagation scenarios, where a wedge shaped PEC obstacle is located in between the transmitter and receiver. The scenario is pictured in Fig. 1.45. Here, the obstacle has a 50-m base length and is 250 m away from a 150-MHz source, which is 25 m above the ground. The height of the obstacle is a parameter.

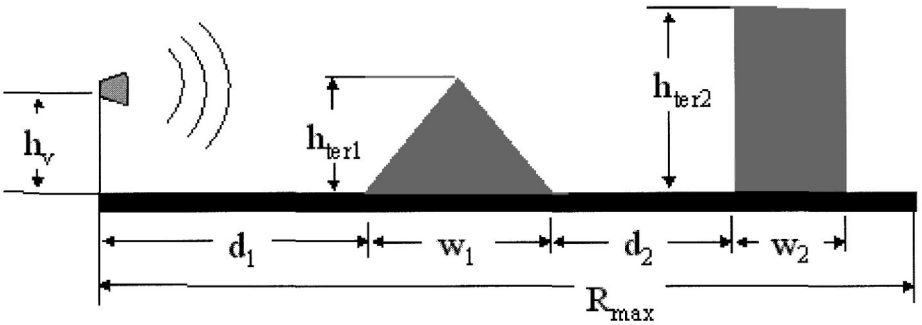

Figure 1.44: *The scenario of the SSPE.INP file in SSPE.INP given above*

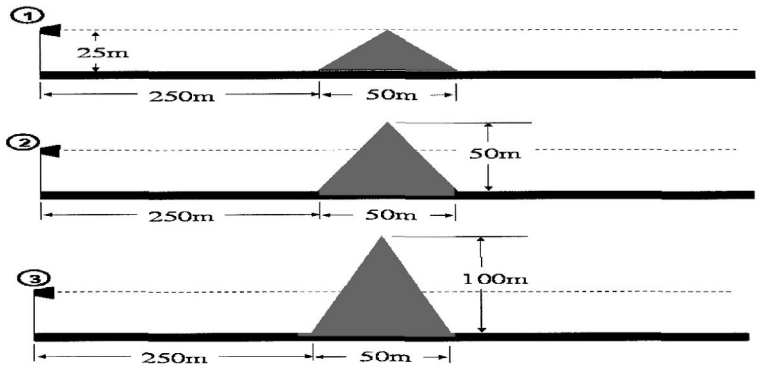

Figure 1.45: *A (first) scenario with single obstacle*

SSPE is run with this scenario and propagation factor vs. both range and height behind the obstacle are calculated. In Fig. 1.46, propagation factor vs. range for the three cases mentioned in Fig. 1.45, are plotted.

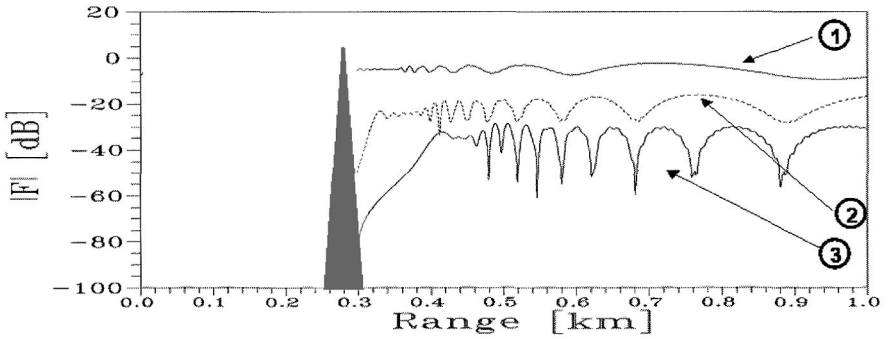

Figure 1.46: *$|E/E_0|$ vs. range for the first scenario (observation height = 25 m)*

As observed from the figure, the higher the obstacle, the lower the signal strength right behind when the receiver height is less than the obstacle. The interested reader may run this scenario with different heights and ranges and could see the differences. The second calculation with this first scenario is done for propagation factor vs. height, and results are given in Fig. 1.47.

The second scenario used as an example in SSPE includes wedge-shaped obstacles with same height but different base lengths. All other parameters are kept the same as in the first scenario (obstacle, and observation heights are 50 m, and 25 m, respectively. Propagation factor vs. range behind the obstacle is given in Fig. 1.48. SSPE and KNIFE simulators can also be compared with each other, since both can handle wedge-type obstacle effects under Dirichlet-type boundary conditions. A comparison at 500 MHz for a 100-m height sharp wedge-type PEC obstacle is given in Fig. 1.49. The scenarios are also pictured in the figure.

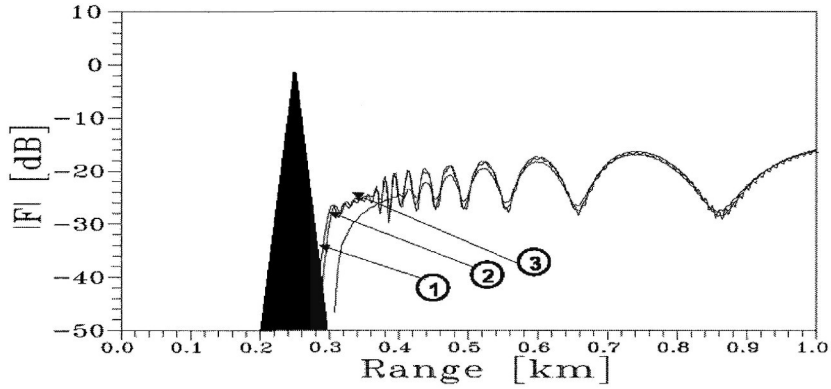

Figure 1.47: *$|E/E_0|$ vs. height for the first scenario (observation range = 25 m)*

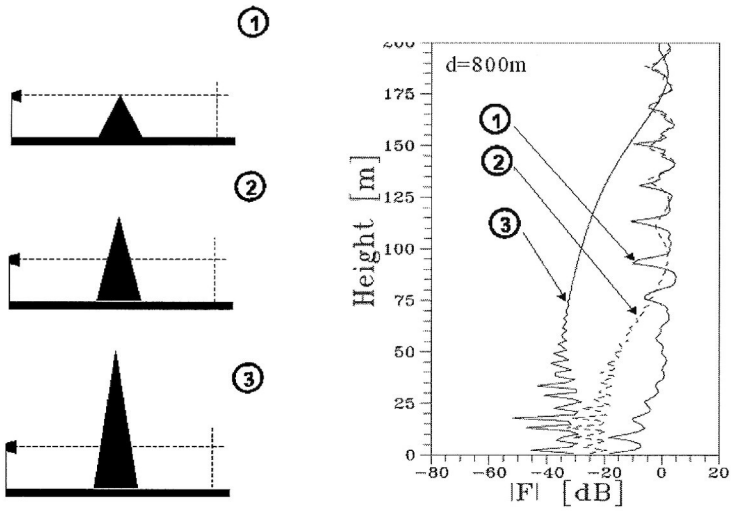

Figure 1.48: *$|E/E_0|$ vs. range for the first scenario (observation height = 25 m) with different base length (1, 50 m; 2, 100 m; 3, 200 m)*

Although the examples starting from Fig. 1.43 to Fig. 1.48 are generated via the SSPE package, some modifications in default parameters (e.g., maximum height) are done to satisfy the accuracy requirements. The contour plots (i.e., propagation factor vs. range/height) are shown in Figs. 1.50 and 1.51 in order to emphasize the importance of parameter selection. In both figures, operating frequency, transmitter-to-wedge distance, and wedge and transmitter heights are selected as 300 MHz, 1000 m, 100 m and 50 m, respectively. In order to show the effect of terrain slope, the wedge base lengths are chosen differently, 2000 m and 100 m for the scenarios shown in Figs. 1.50 and 1.51, respectively. For both scenarios, maximum height is kept as given inside the SSPE package. The color bar at the right side of the figures scales the amplitude of propagation factor. The effect of the obstacle is clearly observed in Fig. 1.50, the propagating wave is scattered from the left edge, and there exists a shadow region behind the wedge. However, in Fig. 1.51, it seems as if the upper part of the wedge permits the wave to penetrate, which is not physically true. The wedge affects as if it is lower. The reason is the slope angle, which is very high compared to the one in Fig. 1.51. Therefore, smaller height step sizes have to be used to satisfy the Nyquist criteria. Besides, staircase terrain approximation in SSPE has difficulties in modeling sharp slopes and needs more diligent discretization in height.

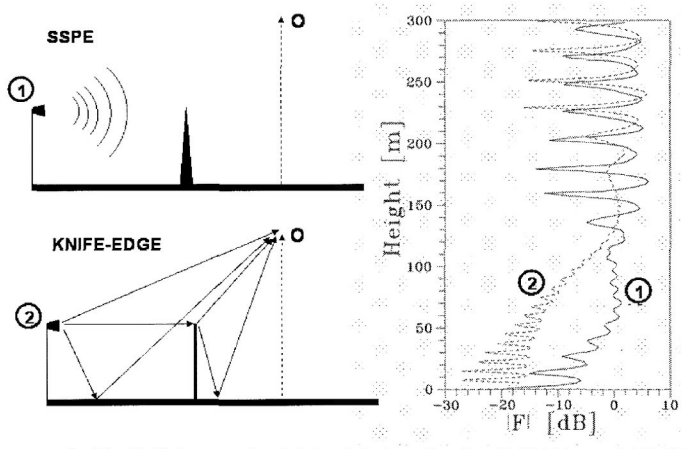

Figure 1.49: *$|E/E_0|$ vs. height obtained with SSPE and KNIFE*

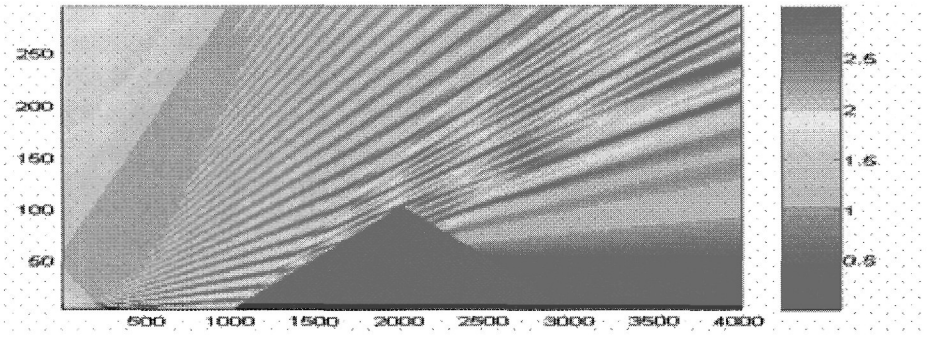

Figure 1.50 *$|F|$ vs. range/height at 300 MHz for wedge with 2000 m base length*

At the upper left of the Figs. 1.50 and 1.51, the amplitude of propagation factor is higher than it should be, because the propagating wave cannot reach that height at that range and numerical error is slightly smaller for free space, causing the denominator in the formula of the propagation factor to be small.

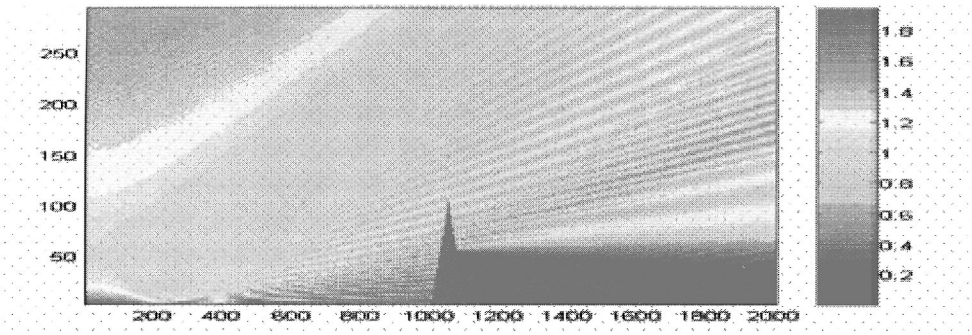

***Figure 1.51**: |F| vs. range/height at 300 MHz for wedge with 100 m base length*

1.5.5 TDWP: Time- Domain Wave Propagator

A simplified version of the TDWP package for HED, where H_x, H_z and E_y are the related field components, is prepared and presented here. In this version:

- The sliding window technique is removed and only a single window is allowed. Therefore, the code is reduced to a 2D TE_z (with no variation along *y*-direction) FDTD code.
- The propagation domain is terminated by 16-PML blocks from left, right, and top. Ground is assumed to be PEC.
- The computation domain is 500 × 2000 with $\Delta x = \Delta y = \Delta z = 10$ cm, which corresponds to a 50-m-high by 200-m-long area.
- The source bandwidth is chosen as B =100 MHz.

The structure of the TDWP, shown in Fig. 1.52, is quite similar to the other propagators. Nevertheless two TD simulations explained below should be run separately in order to calculate propagation factors. Both programs accept the user-supplied input parameters from the same file named as TDWP.INP. But the for the rest of the input parameters, each program needs a different additional parameter file.

- **TDWP-F**: Free space simulation. The additional input parameter file is TDWP-F. PAR. The outputs are given in T-RANGE-F.dat and T-HEIGHT-F.dat files for range and height profiles, respectively.

- **TDWP-S**: Includes obstacles, PEC ground, and refractivity. The additional input parameter file is TDWP-S. PAR. The outputs are given in T-RANGE-S.dat and T-HEIGHT-S.dat files for range and height profiles, respectively. Electric field data vs. height/range are stored in SNAP.DAT in order to plot instant snapshots. An off-line Matlab file (PLOT3D.M) uses SNAP.DAT to depict a 3D figure where electric field variation vs. range/height is shown.

Off-line DFT is applied to the data in these output files, and propagation factor vs. range or height are calculated for a given frequency. The FD data are given in F-RANGE.dat and F-HEIGHT.dat files. Since short pulse propagation is simulated in TDWP, off-line DFT may be applied as many frequencies as the user desires (within bandwidth of the short pulse injected). Necessary input parameters are listed in Table 1.6.

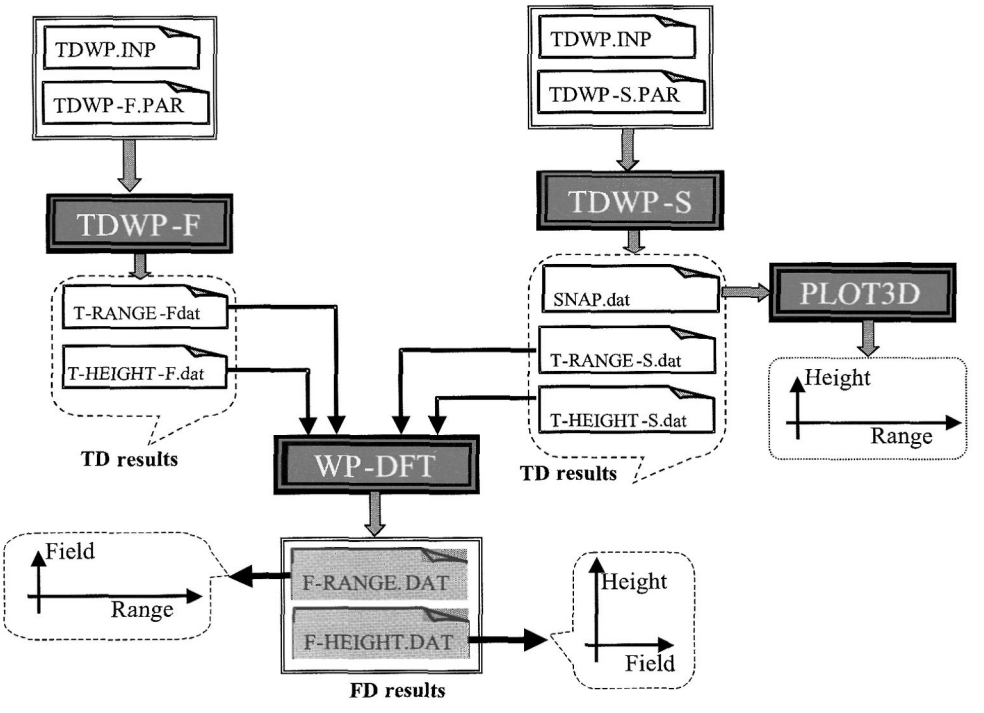

Figure 1.52: *The structure of TDWP package*

For example, the TDWP.INP file given below belongs to Fig. 1.48. The parameters read are transmitter height h_t = 20 m; receiver height h_r = 20 m; single obstacle; observation ranges: 50 m, 100 m, 150 m; obstacle height h_{ter} = 20 m, source-to-obstacle distance d_1 = 50 m; obstacle base; w_1 = 25 m, obstacle: wedge; vertical refractivity profile: standard atmosphere; time steps for instant snapshots: 500 and 1000.

TDWP.INP (Fig. 1.48)	LINE 1:	10
	LINE 2:	10
	LINE 3:	3, 50, 100, 150
	LINE 4:	1
	LINE 5:	20, 50, 25 ,1
	LINE 5	1
	LINE 6	1
	LINE 7	2, 500, 1000

Table 1.6: The TDWP.INP file and required parameters

Row No:	Parameter
1	Transmitter height [m]
2	Receiver (observer) height [m]
3	NRANGE (number of observation ranges: 1 - 3), first observation range [m], second observation range [m] (arbitrary if NRANGE < 2), third observation range [m] (arbitrary if NRANGE < 3)
4	**Scenario type [0, 2]** **(0, no obstacle; 1, single obstacle; 2, double obstacle**
5	**If scenario type is 1 (single obstacle)** Obstacle height [m], source-to- obstacle distance [m], obstacle base length [m], obstacle type (1, wedge; 2, block)
6	**If scenario type is 2 (double obstacle)** Obstacle height [m], source-to- obstacle distance [m], obstacle base length [m], obstacle type (1, wedge; 2, block) Obstacle height [m], distance between two obstacles [m], obstacle base length [m], obstacle type (1, wedge; 2, block)
6 (or 7)	Refractivity profile (1,2 or 3) 1: Standard atmosphere (117) 2: Sub-refraction (200) 3: Super-refraction (-43)
8	N_TIME (number of instant snapshots: 1, 3), first snapshot time [1-NSTOP], second snapshot time [0-NSTOP] (arbitrary if N_TIME < 2), third second snapshot time [0-NSTOP] (arbitrary if N_TIME < 3). Here, NSTOP is the number of total time steps in TDWP. Instant snapshots are available only for TDWP-S.

Like SSPE in FD, TDWP may also be used to obtain 3D plots of propagation directly in TD. An example of this is given in Fig. 1.53, where four different snapshots are plotted.

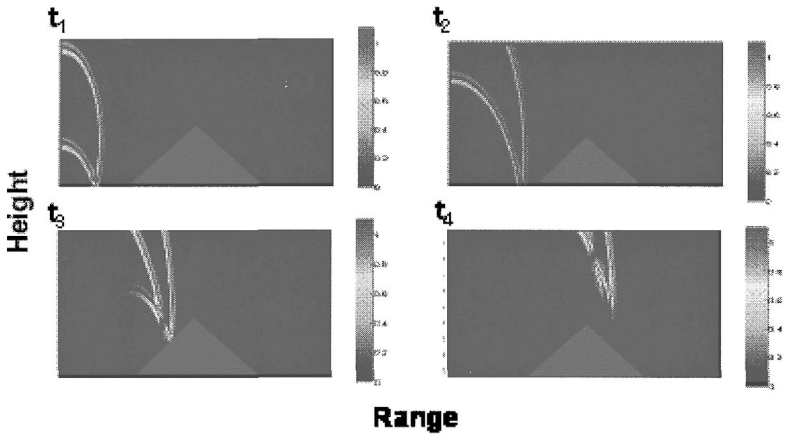

Figure 1.53: *Pulse propagation in TD simulated with TDWP*

CONCLUSIONS AND DISCUSSION

The problem of ground-wave propagation over a non-flat, imperfect earth's surface through a non-homogeneous atmosphere is discussed in this chapter. Three methods are presented; analytical approximate (ray-mode) solutions, the SSPE in FD and the TDWP in TD.

The main conclusions of this chapter are the following:

- Analytical ray-mode techniques (also their hybridized form WAVEPROB) yield sufficiently accurate results only when propagation over a spherical smooth earth (including lossy ground) is considered.

- SSPE is efficient and reliable for modeling narrow-band wave propagation (especially for frequencies VHF and above) over weakly back-scattering rough surfaces, above which exists a vertically and/or horizontally varying refractivity profile.

- The TDWP provides an efficient and reliable method for ground-wave propagation problems involving broadband pulse signals. Although computationally expensive and not yet optimized, this technique is quite flexible and can be used in a variety of applications. By adding decision-makers and parallel processing, the TDWP may be capable of simulating not only 2D but also 3D propagation of pulsed signals over terrain, which may include surface impedance variations.

- Major factors that at present restrict the applicability and/or validity of TDWP are
  (i) computer memory and speed requirements,
  (ii) unwanted reflections from the top PML boundary,
  (iii) numerical dispersion effects.

The restrictions of all these methods are listed in Table 1.7. Also, the comparisons in terms of ground-wave propagation requirements in order to clarify the utilities are listed in Tables 1.8.

Table 1.7: Comparison of the algorithms in terms of operating frequency

Operating Frequency	Ray-Mode (WAVEPROB)	**SSPE**	**TDWP**
MF	Easy	Difficult	Easy
HF	Easy	Difficult	Easy
VHF	Easy	Easy	Difficult
MW	Easy	Easy	Difficult

Most of the numerical results given in this chapter were performed via a personal computer (PCs, Pentium II with 128 MB RAM). The restrictions mentioned in (i) and (iii) above can partly be removed when more capable computers (with larger memory and higher speed) are used. This will allow one to utilize a larger computation space

(as well as a larger sliding window) than that we have used in this study and hence extend the simulation range. At this stage, TD simulators are limited to ranges up to few thousands of wavelengths. The effects of unwanted reflections from the top PML boundary dominate the numerical dispersion effects in most of the propagation scenarios considered in this study. Also, PML works better for propagation over irregular terrain, because of the wide spread scattering of the waves. However, in this case, due to direct and ground scattered pulse interference together with numerical dispersion accuracy deteriorates at longer ranges. On the other hand, some signal processing techniques (such as windowing, signal estimation, etc.) can be incorporated to the TDWP to achieve a (slight) improvement in performance.

Table 1.8: Comparison of the algorithms in terms of ground-wave propagation requirements

Propagation Scenario	Ray-Mode (WAVEPROB)	**SSPE**	**TDWP**
Atmosphere	Standard atmosphere with and without earth's curvature	All kinds of vertical and horizontal atmospheric changes including ducts, but for relatively small atmospheric gradient.	No restriction
Non-flat terrain effects	Only rough surface	All terrain types can be included, but for piecewise linear approximation there exists a limitation for slope angles, and for staircase approximation it is difficult to apply Neumann type surface boundary condition.	No restriction
Surface impedance oundary	Easy	Easy, but there are problems for the source located at a highly conducting surface, such as sea.	Easy, but needs extra calculations if recursive convolution algorithm is applied.
Back and up scattering	Not applicable	Not applicable (possible with finite difference PE or vector PE).	Local back and up scatter effects are included.
Long-range propagation	Easy	Easy	Difficult and needs extra precautions.

References

[1] J. R. Wait, "The Ancient and Modern History of EM Ground-Wave Propagation", *IEEE Antennas and Propagation Magazine*, Vol.40, pp. 7 - 24, 1998

[2] N. DeMinco, "Propagation Prediction Techniques and Antenna Modeling (150 to 1705khz) for Intelligent Transportation Systems (ITS) Broadcast Applications, *IEEE Antennas and Propagat. Magazine*, Vol. 42, pp. 9 - 33, 2000

[3] J. R. Wait, *Electromagnetic Waves in Stratified Media*, Pergamon, Oxford, 1962

[4] V. A. Fock, *Electromagnetic Diffraction and Propagation Problems*, Pergamon, Oxford, pp.191 - 235, 1965

[5] G. Millington, "Ground Wave Propagation over an inhomogeneous smooth earth", *Proc. IRE*, Vol. 96 No. 39, pp. 53 - 64, 1949

[6] R. H. Ott, L. A. Berry, "An alternative integral equation for propagation over irregular terrain", *Radio Science*, Vol. 5, pp. 767 - 771, 1970

[7] R. H. Ott, L. A. Berry, "An alternative integral equation for propagation over irregular terrain", 2, *Radio Science*, Vol. 6, pp. 429 - 435, 1971

[8] K. A. Norton, "The Propagation of Radio Waves over the Surface of Earth and in the Upper Atmosphere", *Proc. IRE*, Vol.24, pp.1367 - 1387, 1936

[9] T. Ishihara, L. B. Felsen, "Hybrid Ray-mode Parameterization of High Frequency Propagation in an Open Waveguide with Inhomogeneous Transverse Refractive Index: Formulation and Application to a bilinear Surface Duct", *IEEE Transactions on Antennas and Propagat.* Vol. 39 No. 6, pp. 780 - 788, 1991

[10] T. Ishihara, L. B. Felsen, "Hybrid Ray-mode Parameterization of High Frequency Propagation in an Open Waveguide with Inhomogeneous Transverse Refractive Index: Numerical results and Quality Assessment", *IEEE Transactions on Antennas and Propagat.* Vol. 39 No. 6, pp. 789 - 797, 1991

[11] L. Sevgi, L. B. Felsen, "A new Algorithm for Ground Wave Propagation Based on a Hybrid Ray-Mode Approach", *Int. J. of Numerical Modeling*, Vol.11 No 2, pp. 87 - 103, March 1998

[12] L. B. Felsen, L. Sevgi, "Adiabatic and Intrinsic Modes for Wave Propagation in Guiding Environments with Longitudinal and Transverse Variations: Formulation and Canonical Test", *IEEE Transactions on Antennas and Propagat.* Vol. 39 No. 8, pp. 1130 - 1136, Aug. 1991

[13] L. B. Felsen, L. Sevgi, "Adiabatic and Intrinsic Modes for Wave Propagation in Guiding Environments with Longitudinal and Transverse Variations: Continuously Refracting Media", *IEEE Transactions on Antennas and Propagat.* Vol. 39 No. 8, pp. 1137 - 1143, Aug. 1991

[14] M. Levy, *Parabolic Equation Methods for Electromagnetic Wave Propagation*, IEE, Institution of Electrical Engineers, 2000

[15] G. D. Dockery, J. R. Kuttler, "An Improved Impedance Boundary Algorithm for Fourier Split-step Solutions of the Parabolic Wave Equation", *IEEE Transactions on Antennas and Propagat.* Vol. 44 No. 12, pp. 1592 - 1599, 1996

[16] T. Ishihara, L. B. Felsen, "Hybrid Ray-Parabolic Equation analysis of Propagation in Ocean Acoustic Guiding Environments", *J. Acoust. Soc. Am.*, Vol. 83, pp. 950 - 960, 1988

[17] W. Marcus, "A Hybrid (Finite Difference-Surface Green's function) method for computing Transmission Losses in an Inhomogeneous Atmosphere Over Irregular Terrain", *IEEE Transactions on Antennas and Propagat.* Vol. 40 No. 12, pp. 1451 - 1458, Dec. 1992

[18] F. Akleman, L. Sevgi, "A Novel Time-domain Wave Propagator", *IEEE Transactions on Antennas and Propagat.* Vol. 48 No. 5, pp. 839 - 841, 2000
[19] F. Akleman, L. Sevgi, "Realistic Surface Modeling in a Time-domain Wave Propagator ", IEEE Transactions on Antennas and Propagation, (to appear) July 2003
[20] M.O. Özyalçın, F. Akleman, L. Sevgi, "A TLM Based Novel Time Domain Ground Wave Propagator", *IEEE Transactions on Antennas and Propagat.* (to appear) June 2003
[21] J. Deygout, "Correction Factor for Multiple Knife-edge Diffraction", *IEEE Trans. Antennas and Propagat. Vol.* 39, pp. 1256 - 1258, Aug. 1991
[22] R. J. Luebbers, "Propagation Prediction for Hilly Terrain Using GTD Wedge Diffraction", *IEEE Transactions on Antennas and Propagat.* Vol. 32, pp. 951 - 955, 1984
[23] J. H. Whitteker, "Fresnel-kirchhoff Theory Applied to Terrain Diffraction Problems", *Radio Science*, Vol. 25, pp. 837 - 851, 1990
[24] J. T. Hviid, J.B. Andersen, J. Toftgard, J. Bojer, "Terrain-based Propagation Model for Rural Area – An Integral Equation Approach", *IEEE Transactions on Antennas and Propagat.*, Vol. 43, pp. 41 - 46, Jan. 1995
[25] L. Sevgi, F. Akleman, L. B. Felsen, "Ground Wave Propagation Modeling: Problem-Matched Analytical Formulations And Direct Numerical Techniques", *IEEE Antennas and Propagation Magazine*, Vol. 44 No.1, pp. 55 - 75, 2002
[26] M. P. Shatz, G. H. Polychronopoulos, "An Algorithm for the Evaluation of Radar Propagation in the Spherical Earth Diffraction Region", *IEEE Transactions on Antennas and Propagat.,* Vol.38 No. 8, pp.1249 - 1252, 1990
[27] D. E. Kerr (ed.), *The Propagation of Short Radio Waves*, Radiation Lab. Series, Vol. 13, McGraw-Hill, Ne York, 1951
[28] M. P. M. Hall, L. W. Barclay, M. T. Hewitt (ed.), *Propagation of Radiowaves*, IEE Press, London, 1996
[29] E.C. Jordan, K. G. Balmain, *Electromagnetic Waves and Radiating Systems*, Prentice-Hall, Englewood Cliffs, NJ, 1968
[30] M. Abramowitz, I.A. Stegun, *Handbook of Mathematical Functions*, Dover, 1969
[31] F.D. Tappert, The Parabolic Approximation Method in *Wave Propagation and Underwater Acoustics*, pp. 224-287 (Eds.) J. B. Keller and J. S. Papadakis Springer-Verlag, New York, 1977.
[32] F.R Di Napoli and R.L. Daevenport, Numerical Methods of Underwater Acoustic Propagation in *Numerical methods of Underwater Acoustic propagation*, J. A DeSanto (Ed.), Springer-Verlag, New York, 1977.
[33] J. R. Kutler and G. D Dockery,. "Theoretical Description of the Parabolic Approximation / Fourier Split Step Method of Representing Electromagnetic Propagation in the Troposphere", *Radio Science*, Vol. 26, pp. 381 - 393. 1991
[34] L. Sevgi, E. Topuz, "Split step Parabolic Equation analysis of Coupled Dielectric Waveguides", ELEKTRIK, Turkish J. of Electronics and Communication, Vol. 3 No 2-3, pp. 85 - 92, 1995
[35] L. Sevgi, "Split Step Parabolic Equation Solutions in Surface Duct-to-Elevated Duct Transition", Turkish J. of Physics, Vol. 19 No. 3, pp. 541 - 551, 1995
[36] D. J. Thomson and N. R Chapman "A Wide-Angle Split-Step Algorithm for the Parabolic Equation", *J. Acoust. Soc. Am.*, Vol. 74, pp. 1848 - 1854, 1993
[37] M. D Collins, "A Split Step Pade Solution For The Parabolic Equation Method", *J. Acoustic. Soc. Am.*, Vol. 94, pp.1736-1742, 1993

[38] F. Akleman, *Time and Frequency Domain Numerical Modeling of Ground Wave Propagation*, Ph.D Thesis, Istanbul Technical University, July 2002, Istanbul, Turkey

[39] K. S. Yee, "Numerical Solution of Initial Boundary Value Problems Involving Maxwell's equations," *IEEE Transactions on Antennas and Propagat*, Vol. 14 No. 3, pp. 302 - 307, May 1966

[40] C. Christopoulos, *The transmission-line modeling method*, Oxford University Press, Oxford, 1995

[41] C. Eswarappa, W. J. R. Hoefer, "Implementation of Berenger Absorbing Boundary Conditions in TLM by Interfacing FDTD Perfectly Matched Layers", *Electronic Letters*, Vol. 31 No. 15, pp. 1264 - 1266, 1995

[42] J. H. Beggs, R. J. Luebbers, K. S. Yee, K. S. Kunz, "Finite-Difference Time-Domain Implementation of Surface Impedance Boundary Conditions", *IEEE Transactions on Antennas and Propagat*, Vol. 40 No. 1, pp. 49 - 56, 1992

[43] M. L. Meeks, *Radar Propagation at low Altitudes*, Artech House, Boston, MA, 1982

[44] CCIR, "Ground Wave Propagation Curves for Frequencies Between 10 kHz and 30 MHz", *CCIR Rec.* 368-6, 1990